

This manuscript represents a post-print that has been accepted for publication in the *Journal of Petrology* following peer-review (submitted 24th of August 2020).

1 **This manuscript has now been accepted for publication in *Journal***
2 ***of Petrology*. The published version of the manuscript can be found**
3 **here: <https://doi.org/10.1093/petrology/egaa094>**

4 **Please cite this manuscript as:**

5 Matthew L M Gleeson, Sally A Gibson, Michael J Stock, Upper Mantle Mush
6 Zones beneath Low Melt Flux Ocean Island Volcanoes: Insights from Isla
7 Floreana, Galápagos, *Journal of Petrology*, Volume 61, Issue 11-12, December
8 2020, egaa094, <https://doi.org/10.1093/petrology/egaa094>

9

Upper mantle mush zones beneath low melt flux ocean island volcanoes: insights from Isla Floreana, Galápagos

Matthew L. M. Gleeson^{1,2*}, Sally A. Gibson¹ and Michael J. Stock^{1,3}

¹Department of Earth Sciences, University of Cambridge, Downing Street, CB2 3EQ, UK

²School of Earth and Ocean Sciences, Cardiff University, Park Place, Cardiff, CF10 3AT, UK

³Department of Geology, Trinity College Dublin, College Green, Dublin 2, Ireland.

*Corresponding author email address: matthew.gleeson.geo@gmail.com

ABSTRACT

The physicochemical characteristics of sub-volcanic magma storage regions have important implications for magma system dynamics and pre-eruptive behaviour. The architecture of magma storage regions located directly above high buoyancy flux mantle plumes (such as Kīlauea, Hawai'i and Fernandina, Galápagos) are relatively well understood. However, far fewer constraints exist on the nature of magma storage beneath ocean island volcanoes that are distal to the main zone of mantle upwelling or above low buoyancy flux plumes, despite these systems representing a substantial proportion of ocean island volcanism globally. To address this, we present a detailed petrological study of Isla Floreana in the Galápagos Archipelago, which lies at the periphery of the upwelling mantle plume and is thus characterised by an extremely low flux of magma into the lithosphere. Detailed *in situ* major and trace element analyses of crystal phases within exhumed cumulate xenoliths, lavas and scoria deposits, indicate that the erupted crystal cargo is dominated by disaggregated crystal-rich material (i.e., mush or wall rock). Trace element disequilibria between cumulus phases and erupted melts, as well as trace element zoning within the xenolithic clinopyroxenes, reveals that reactive porous flow (previously identified beneath mid-ocean ridges) is an important process of melt transport within crystal-rich magma storage regions. In addition, application of three petrological barometers reveal that the Floreana mush zones are located in the upper mantle, at a depth of 23.7 ± 5.1 km. Our barometric results are compared to recent studies of high melt flux volcanoes in the western Galápagos, and other ocean island volcanoes worldwide, and

37 demonstrate that the flux of magma from the underlying mantle source represents a first-order control
38 on the depth and physical characteristics of magma storage.

39 **KEY WORDS**

40 Galápagos; magma storage; reactive porous flow; barometry.

41 **1 INTRODUCTION**

42 The physicochemical characteristics (such as size, pressure, volatile content and geochemical
43 heterogeneity) of magma storage at volcanic centres located directly above high buoyancy flux mantle
44 plumes (e.g. Kīlauea, Hawai'i and Isabela, Galápagos) have been subject to intense study over the
45 past few decades (Bagnardi et al., 2013; Bernard et al., 2019; Clague and Denlinger, 1994; Geist et
46 al., 1998; Naumann and Geist, 1999; Neal et al., 2019; Park et al., 2007; Pietruszka et al., 2015;
47 Poland et al., 2015; Sides et al., 2014; Stock et al., 2018; Wieser et al., 2020, 2019). Systems such as
48 Kīlauea are characterised by frequent volcanic activity, and geophysical (seismicity, ground
49 deformation) and geochemical (gas emissions) monitoring is prevalent. Monitoring data, combined
50 with petrological and geochemical analysis of erupted products (mineral textures, deformation
51 characteristics and chemistry) provide important insights into the architecture and dynamics of their
52 sub-volcanic plumbing systems (Amelung et al., 2000; Davidge et al., 2017; Geist et al., 2014;
53 Hartley et al., 2018; McCormick Kilbride et al., 2016). However, these systems (which we term 'high
54 melt flux') represent only one endmember of global plume-derived volcanism. Low melt flux
55 systems, either above low buoyancy flux plumes (e.g. Canary Islands; Longpre et al., 2014) or at
56 volcanic systems distal to the centre of mantle melting at high buoyancy flux mantle plumes (e.g.
57 eastern and south-eastern Galápagos; Harpp and Geist, 2018), are the other endmember.

58 While a substantial number of hotspot-related volcanic systems that have been active during the
59 Holocene are located in regions characterised by a relatively low flux of magma into the lithosphere
60 (i.e., regions distal to the main zone of plume upwelling or above low buoyancy flux plumes; Samoa,
61 Canary Islands, Cape Verde; Global Volcanism Program, 2013), only a small number of eruptions
62 have been observed (and recorded) at these systems since the advent of modern volcano monitoring

63 techniques. As a result, few constraints exist on the conditions of magma storage in regions
64 characterised by a low flux of magma into the lithosphere, relative to volcanic centres located above
65 the centre of mantle plumes with a large buoyancy flux (and thus generating a large flux of magma
66 and more frequent eruptions).

67 The flux of mantle-derived magma into the lithosphere is thought to impart a first-order control on the
68 evolution of ocean island volcanoes and the homogeneity of erupted liquids (Geist et al., 2014).

69 Therefore, placing constraints on the physicochemical characteristics of magma storage at low melt
70 flux ocean island volcanoes is essential for determining the influence of mantle dynamics and melt
71 generation processes on the structure and physical characteristics of sub-volcanic magma plumbing
72 systems. In the absence of detailed monitoring data, petrological and geochemical analyses of
73 volcanic products from past eruptions represent the only available tools for determining the structure
74 and processes operating within these systems, as well as possible eruption precursors.

75 Isla Floreana in the south-eastern Galápagos is currently located ~100 km downstream from where the
76 centre of the Galápagos plume impacts on the base of the lithosphere beneath the island of Isabela in
77 the western archipelago (Fig. 1; Villagómez et al., 2014). Hence, although the Galápagos plume has a
78 relatively high buoyancy flux compared to regions such as the Canary Islands (Jackson et al., 2017),
79 Floreana's location relative to the main zone of mantle plume upwelling results in an extremely low
80 flux of magma entering the lithosphere and, consequently, very infrequent volcanic activity (Harpp et
81 al., 2014a; Harpp and Geist, 2018). Floreana is considered to be an infrequently active volcanic
82 centre, rather than extinct, owing to the persistent volcanic activity since ~1 Ma and the long-lived
83 nature of volcanism on the eastern Galapagos islands that lie >100 km 'downstream' of the Galapagos
84 mantle plume (e.g. the youngest lavas on San Cristobal are ~9 ka; Mahr et al., 2016).

85 In this paper, we present a thorough petrological study of scoria, lava and xenolith samples from
86 Floreana and place constraints of the structure, depth and crystallinity of magmatic systems beneath
87 this low melt flux ocean island volcano. We compare our results with more frequently active volcanic
88 centres in the western Galápagos (near the centre of plume upwelling; Geist et al., 1998; Naumann
89 and Geist, 1999; Stock et al., 2018), as well as other ocean island volcanoes worldwide (Hammer et

90 al., 2016; Hartley et al., 2018; Poland et al., 2015), to investigate how the flux of magma into the
91 lithosphere influences the depth and crystallinity of sub-volcanic magma storage regions.

92 **2 GEOLOGICAL BACKGROUND**

93 The Galápagos Archipelago in the eastern equatorial Pacific is one of the most volcanically active
94 regions on Earth, with eruptions typically occurring every 2–3 years (Global Volcanism Program,
95 2013). Although most historic Galápagos eruptions have taken place on the two westernmost islands
96 of Isabela and Fernandina (Fig. 1), infrequent volcanic activity has also occurred on several islands in
97 the eastern and south-eastern Galápagos (for example, Santiago in 1906 and Marchena in 1991;
98 Global Volcanism Program, 2013). In fact, volcanic activity in the eastern Galapagos, >100 km
99 ‘downstream’ of the postulated position of the plume stem, has been shown to be long-lived, with
100 volcanic activity on San Cristobal extending over 2 Myrs with the most recent lavas erupted at ~9 ka
101 (Mahr et al., 2016).

102 Volcanoes in the western Galápagos likely emerged within the last 500 kyr (Naumann and Geist,
103 2000), whereas those in the eastern and south-eastern Galápagos are considerably older (eruption ages
104 up to 2.3 Ma and 3.2 Ma have been measured on San Cristobal and Espanola, respectively; Bailey,
105 1976; Geist et al., 1986). In addition, substantial differences in geomorphology and the style of
106 volcanic activity are observed across the archipelago (Geist et al., 1995; Harpp et al., 2014a; Harpp
107 and Geist, 2018). For example, volcanoes in the western archipelago are typified by large summit
108 calderas (<700m deep), which are not present on the eastern islands (Chadwick and Howard, 1991;
109 Cleary et al., 2020; Harpp and Geist, 2018).

110 Geochemical distinctions between the western and eastern/south-eastern Galápagos islands are also
111 observed, which are primarily related to variations in the composition of the underlying mantle source
112 (Geist et al., 1988; Gibson and Geist, 2010; Gleeson et al., 2020; Harpp and White, 2001; White et al.,
113 1993) or the volume flux of mantle-derived magma that ascends into the lithosphere (Geist et al.,
114 1995, 2014; Gibson et al., 2016; Harpp and Geist, 2018). For example, variations in the flux of mantle
115 derived magma are hypothesised to influence the geochemical heterogeneity of erupted basalts at each

116 island: volcanoes in the western archipelago typically erupt a very narrow range of basaltic
117 compositions over hundreds of millennia during their main shield building phase, whereas basalts
118 erupted from a single island in the eastern and/or south-eastern archipelago, such as Floreana, tend to
119 display far greater compositional heterogeneity (Geist et al., 2014; Harpp and Geist, 2018).

120 Floreana is characterised by numerous scoria cones and blocky, heavily vegetated lava flows that can
121 typically be traced to the cone from which they originated (Bow and Geist, 1992; Harpp et al., 2014a).
122 The crustal thickness beneath Floreana is ~16 km, similar to that observed in the western Galápagos
123 10–18 km (Feighner and Richards, 1994), and the lithospheric thickness beneath the western and
124 south-eastern Galápagos is very similar (~50–60 km; Gibson and Geist, 2010). Recent work has
125 shown that the average volumetric eruption rate on Floreana over the past 1–1.5 Myrs is 1–10 m³·yr⁻¹,
126 6 orders of magnitude lower than the current volcanic productivity at volcanoes in the western
127 Galápagos (cf. ~4.4·10⁶ m³·yr⁻¹ at Fernandina; Harpp et al., 2014a; Kurz et al., 2014). This difference
128 in volumetric eruption rate likely reflects a substantially lower flux of magma into the lithosphere
129 beneath Floreana than beneath each volcanic centre in the western Galápagos.

130 Despite the relatively low volcanic productivity of Floreana over the last ~1–1.5 Myrs, the erupted
131 products have several important characteristics that provide insights into the nature of the underlying
132 magmatic system. For example, Floreana has a high proportion of pyroclastic deposits compared to
133 the other Galápagos islands (Harpp et al., 2014a) and eruption deposits typically contain a large
134 number of cumulate xenoliths (Bow and Geist, 1992; Lyons et al., 2007), which have been interpreted
135 as evidence for very high magma ascent rates (Harpp et al., 2014a).

136 Floreana is the only Galápagos island that displays evidence for multiple stages in its volcanic
137 evolution. Submarine parts of the island have isotopic and trace element characteristics that are
138 similar to those measured in recent basalts erupted on southern Isabela, near the centre of plume
139 upwelling (e.g. Sierra Negra and Cerro Azul, Fig. 1A), whereas the subaerial material is isotopically
140 distinct (high ²⁰⁶Pb/²⁰⁴Pb and ⁸⁷Sr/⁸⁶Sr ratios; Harpp et al., 2014). The trace element and isotopic
141 differences between the erupted basalts is mirrored in xenoliths found in the Floreana lava and scoria
142 deposits: gabbroic xenoliths have radiogenic isotope ratios that are similar to modern Isabela basalts,

143 whereas wehrlitic xenoliths have trace element and isotopic compositions that resemble recent
144 Floreana subaerial basalts (Lyons et al., 2007). Differences in the isotopic characteristics of the
145 Floreana lavas (submarine vs subaerial) and xenoliths (gabbros vs wehrlites) are thought to indicate a
146 change in the mean composition of magma produced by mantle melting beneath the island at ~1–1.5
147 Ma (Harpp et al., 2014a). In this study, we focus on constraining the depth and physical
148 characteristics of magma storage during the most recent period of volcanic activity on Isla Floreana
149 (<1–1.5 Ma) using chemical and textural analysis of crystal phases in lava flows and xenolithic
150 nodules.

151 **3 SAMPLES AND PETROGRAPHY**

152 The Floreana samples analysed in this study consist of lavas (27 samples), scoria (2 samples) and
153 xenoliths (4 wehrlite, 3 dunite and 2 gabbro samples; Fig. 1B). Most lava samples were collected from
154 the unaltered, low vesicularity cores of blocky flows or glassy flow fronts. All samples form part of
155 the Main Series of Floreana lavas identified by Bow and Geist (1992). The scoria samples were
156 collected from two separate deposits and comprise rapidly cooled scoria lapilli (~0.5–2 cm across;
157 17MMSG16) and bombs (~10 cm across; 17MMSG20). Xenolithic fragments (3–15cm across) were
158 sampled from two different scoria cones on the north-east coast of Floreana; similar xenoliths are also
159 found within most lava flows across the entire island (Supplementary Information).

160 **3.1 Lavas and scoria**

161 The lava and scoria samples analysed in this study are typically olivine phyric with minor anhedral
162 clinopyroxene and very rare orthopyroxene. Except for small plagioclase laths in the microcrystalline
163 groundmass, plagioclase crystals are extremely rare in the Floreana lavas. Plagioclase macrocrysts are
164 only present in one of our lava samples (17MMSG29) where they occur as isolated phenocrysts and in
165 plagioclase-olivine crystal clots (Table S.1). The abundance of olivine and absence of plagioclase in
166 the Floreana lavas and scoria contrasts with basalts in the central, northern, and western parts of the
167 Galápagos Archipelago, where plagioclase-phyric and ultraphyric basalts are common (Geist et al.,
168 2002; Gibson et al., 2012; Harpp et al., 2014b).

169 Despite their relatively simple mineralogy, Floreana lava and scoria samples contain texturally diverse
170 olivine crystals which can be divided into five distinct groups (Fig. 2):

- 171 - Group 1 olivines are present in all lava and scoria samples and are the most abundant type of
172 olivine (~60-70% of all crystals). They are characterised by homogeneous cores, with respect
173 to major elements, and narrow normally zoned rims (Fig. 2A). Group 1 olivines are generally
174 subhedral to euhedral.
- 175 - Group 2 olivines are the second most abundant group (~20-30%) and display reverse zoning.
176 They are typically euhedral, with occasional small embayments (Fig. 2B).
- 177 - Group 3 olivines are also reversely zoned, but are distinguished by skeletal overgrowths,
178 indicating significant undercooling of the host magma and rapid crystal growth (Fig. 2C;
179 Donaldson, 1976; Welsch et al., 2014). Group 3 olivines are less abundant than Groups 1 and
180 2 olivines (<10%).
- 181 - Group 4 olivines are present in low abundance (<10%). They have homogeneous cores and
182 reverse-zoned rims (up to ~300 μm thick). The rims have sieve textures, potentially
183 suggesting resorption and chemical disequilibrium with their carrier melts (Fig. 2D).
- 184 - Group 5 olivines are only found in a minority of samples and are characterised by the
185 presence of 4 compositional zones with alternating high and low forsterite contents (visible in
186 back-scattered electron images; Fig. 2E and F).

187 **3.2 Xenoliths**

188 *3.2.1 Gabbroic xenoliths*

189 Floreana gabbroic xenoliths predominantly comprise plagioclase (33–66 vol.%), clinopyroxene (28–
190 46 vol.%) and orthopyroxene (5–15 vol.%), with little or no olivine (Table S.2). Plagioclase and
191 pyroxene crystals are typically >500 μm and grain sizes are relatively uniform within a single xenolith
192 sample. Where three plagioclase grains meet at a triple junction, 120° grain boundaries indicate a high
193 degree of textural equilibrium (Fig. 3A; Holness et al., 2005). Some of the gabbros have
194 clinopyroxene-rich and plagioclase-rich layers of 2–5 mm thickness.

195 3.2.2 *Dunitic xenoliths*

196 Olivine dominates the dunitic Floreana xenoliths (>90 vol.%). The olivine crystals are subhedral to
197 euhedral and may have undergone partial textural re-equilibration, with some olivine triple junctions
198 approaching 120° grain boundaries. Minor intercumulus clinopyroxene is present along grain
199 boundaries and between pre-existing olivine crystals (Fig. 3B).

200 3.2.3 *Wehrlitic xenoliths*

201 Floreana wehrlitic xenoliths contain olivine (>50 vol.%), clinopyroxene (20–40 vol.%),
202 orthopyroxene (~0–7 vol.%) and minor spinel (<1 vol.%; Table S.2). Clinopyroxene typically occurs
203 as large (<5 mm) oikocrysts, which enclose rounded olivine chadacrysts <500 µm in diameter (Fig.
204 3C and D). Fine-scale orthopyroxene exsolution lamellae (<2 µm) is observed in the clinopyroxenes
205 of a single wehrlite (17MMSG03a; Fig. 3E and F). Olivine grains that are not enclosed by
206 clinopyroxene are typically larger (>1 mm) and more euhedral than the chadacrysts. In some samples,
207 the boundary between clinopyroxene and olivine crystals is characterised by a thin (<20–30 µm) layer
208 of glass and very fine-grained microcrysts. Excluding the rare exsolution lamellae in sample
209 17MMSG03a, orthopyroxene crystals are typically anhedral, infilling the space between earlier
210 formed clinopyroxene and olivine grains. Our observations of dunitic and wehrlitic xenoliths (which
211 have the isotopic signatures of modern day Floreana basalts; Lyons et al., 2007) indicate that the
212 typical order of crystallisation beneath Floreana is olivine, followed by clinopyroxene, with little to no
213 crystallisation of plagioclase.

214 4 ANALYTICAL METHODOLOGY

215 4.1 Electron microprobe analysis

216 Glass chips, olivine and clinopyroxene crystals were hand-picked from crushed scoria and lava
217 samples, mounted in epoxy or indium, and then ground and polished prior to analysis (crystals
218 mounted in indium were polished individually prior to mounting). Xenolithic crystals were analysed
219 as individual crystals mounted in indium or *in situ* in petrographic thin sections. The major and minor
220 element concentrations of olivine, clinopyroxene and glass were measured using a Cameca SX100

221 electron microprobe in the Department of Earth Sciences, University of Cambridge. Calibrations were
222 made using mineral and metal standards prior to each analytical session (see Gleeson and Gibson,
223 2019 for details). Glasses were analysed using a 6 nA, 15 kV, defocused (5 μm) beam for most
224 elements. Na and K were analysed first (10 s peak count time) to avoid alkali migration. Other
225 elements were analysed with peak count times of 10 s (Si), 20 s (Fe), 30 s (Al, P, Ca, Mg), 40 s (Mn),
226 or 60 s (Ti). Sulphur was analysed last using a 20 nA beam current and a 60 s peak count time.

227 Pyroxene compositions were determined by spot analyses using a 20 nA, 15 kV, focused ($\sim 1 \mu\text{m}$)
228 beam, with Na, K and Si analysed first (10 s). Element maps of Cr, Ti, and Al in key clinopyroxene
229 crystals from the Floreana xenoliths were created using a 60 nA, 15 kV, focused ($\sim 1 \mu\text{m}$) beam, with
230 a dwell time of 150 ms. Cr counts were collected on a PET and a LIF crystal, Al counts were
231 collected on two TAP crystals, and Ti counts were collected on a PET crystal. Olivine electron
232 microprobe analysis was carried out using the method outlined in Gleeson and Gibson (2019).

233 Analytical uncertainties were tracked through analysis of appropriate Smithsonian Microbeam
234 Standards (Jarosewich et al., 1980). Accuracy was typically between 98 and 102% for all phases. 2σ
235 analytical precision of clinopyroxene and olivine analyses are typically better than 2–3% for major
236 elements ($>1 \text{ wt}\%$) and typically $\sim 5\text{--}10\%$ for minor elements ($<1 \text{ wt}\%$). Similarly, the 2σ precision for
237 glass analysis was typically $<3\%$ for major elements, $\sim 5\%$ for Na, and $\sim 10\%$ for K (see
238 Supplementary Information).

239 **4.2 Laser ablation Inductively Coupled Plasma Mass Spectrometry**

240 Trace element concentrations were measured in the apparent cores (i.e. as exposed in the 2D plane) of
241 clinopyroxene crystals from scoria and xenolith samples using an ESI193 laser coupled to a Nexion
242 350D inductively coupled plasma mass spectrometer in the Department of Earth Sciences, University
243 of Cambridge. Analyses were collected in spot mode using a 20 Hz laser repetition rate, 4 J/cm^2
244 fluence and $80 \mu\text{m}$ spot size, or in transect mode using a 10 Hz repetition rate, 3.5 J/cm^2 fluence and
245 $30 \mu\text{m}$ spot size. For transects, individual spots were offset into two (alternating) lines to increase the
246 spatial resolution. Laser ablation inductively coupled plasma mass spectrometry (LA-ICP-MS) data

247 reduction was carried out in Iolite[®], with NIST 612SRM as the standard reference material (Hinton,
248 1999) and ⁴³Ca (from electron microprobe analysis) as the internal reference standard. Analytical
249 accuracy was tracked using a USGS glass standard (Jochum et al., 2016) and was between 95% and
250 105% for most elements (See Supplementary File). 2 σ analytical precision of spot analyses were
251 monitored through analysis of an in-house clinopyroxene standard and was 5–10% for the light rare-
252 earth elements (LREE), Y, Sr, and Zr and 10–20% for the heavy rare earth element (HREE). 2 σ
253 analytical precision was ~10% for all elements of interest in transect analyses (Ce, Y).

254 **5 GLASS AND MINERAL CHEMISTRY**

255 **5.1 Matrix glass compositions**

256 The matrix glass compositions measured in one scoria (17MMSG16) and two glassy lava samples
257 (17MMSG12 and 17MMSG27) from Floreana have very similar MgO concentrations (mean
258 concentrations of 6.06–6.67 wt%) but exhibit differences in the concentrations of other elements (Fig.
259 4). For example, sample 17MMSG12 has consistently lower TiO₂ and Al₂O₃ concentrations than
260 17MMSG16, which must either reflect heterogeneity in the composition of primary mantle melts or
261 variations in crustal processing (e.g. the extent of plagioclase or clinopyroxene crystallisation; Fig.
262 4A,D). The largest variation in the glass major element composition, however, is seen in sample
263 17MMSG27 where, at a near constant MgO contents, the CaO, Na₂O, and K₂O contents vary by ~6
264 wt%, 4.5 wt%, and 1.5 wt%, respectively (Fig. 4B,C). Differences between our matrix glass major
265 element analyses and previously-published whole-rock data from Floreana (Harpp et al., 2014a) are
266 primarily due to olivine accumulation in the whole-rock samples (additional accumulation of
267 clinopyroxene may explain the high CaO content of some whole-rock samples; Fig. 4C).

268 Our Floreana matrix glass analyses have higher Al₂O₃ concentrations, at a given MgO content, than
269 basaltic glass and whole-rock measurements from the western Galápagos Archipelago (excluding
270 whole-rock samples with accumulated plagioclase, Fig. 4D; Geist et al., 2002). This indicates
271 substantially lower extents of plagioclase fractionation in the Floreana magmatic system and is
272 consistent with the scarcity of plagioclase phenocrysts in erupted Floreana lavas. Reduced plagioclase

273 crystallisation could be due to the major element composition or H₂O content of primary mantle melts
274 and/or increased pressure of magma storage (Asimow and Langmuir, 2003; Neave et al., 2019;
275 Thompson, 1987; Winpenny and Maclennan, 2011).

276 **5.2 Olivine compositions**

277 Olivine crystals in our Floreana lava and scoria samples show large variations in their forsterite
278 contents (Fo = 70–92, where Fo=(Mg/(Mg+Fe²⁺) molar) with histograms showing a primary density
279 peak at Fo~85 (Fig. 5), more primitive than the olivine compositions in equilibrium with basaltic
280 glasses from Floreana (K_D=0.27-0.34, assuming a Fe³⁺/Fe_{tot} ratio of 0.15; Matzen et al., 2011;
281 Peterson et al., 2015; Roeder and Emslie, 1970). Although there is no clear correlation between Fo
282 and Ca concentration in these crystals, the most forsteritic olivines (Fo>83) have extremely diverse Ca
283 contents (~250 to ~2600 ppm; Fig. 5), whereas crystals with lower Fo contents (<83) have
284 ubiquitously low Ca concentrations (<1500 ppm). All crystals with >1500 ppm Ca are classified as
285 Group 1 olivines. Crystals with <1500 ppm Ca, however, may be classified in any of the 5 olivine
286 groups, with the most evolved crystals (Fo ~70) the only to display the sieve-like rim texture of Group
287 4 olivines.

288 Floreana olivines separated from the lava and scoria samples also have a large range of Ni
289 concentrations (~700 to ~3200 ppm), consistent with crystallisation from a peridotite-derived melt
290 (Fig. 5; Gleeson and Gibson, 2019; Herzberg, 2011; Matzen et al., 2017b, 2017a). All olivine crystals
291 analysed in the wehrlite and dunite xenoliths have a narrow range of Fo contents (83-87) and,
292 crucially, have uniformly low Ca concentrations (<1000 ppm) and moderately high Ni contents
293 (~2000 ppm). Core-rim profiles were performed on a small number of the wehrlitic olivines, revealing
294 typically flat profiles in Fo, Ni, and Ca, with one profile displaying evidence for an increase in Ca in
295 the outer 10 – 20 μm (see Supplementary Information). The range in Ca contents of the Floreana
296 olivines contrasts with isolated olivine crystals from other Galápagos islands where Ca is typically
297 >1000 ppm (Gleeson and Gibson, 2019; Vidito et al., 2013). The Ca and Ni contents of our Floreana
298 olivines are inversely related at a set Fo content (Fig. 5B).

299 **5.3 Clinopyroxene compositions**

300 *5.3.1 Major elements*

301 The Floreana clinopyroxenes separated from the scoria and xenolith samples are augitic, and have a
302 relatively high Mg# (0.85–0.90; Mg# = Mg/(Mg+Fe_i) molar). The clinopyroxenes reach high Na
303 concentrations up to 1.58 wt% Na₂O (0.11 Na atoms per formula unit; Fig. 6A) and, correspondingly,
304 up to 10% of the jadeite component. In general, clinopyroxene separates from scoria samples display
305 a wide range of Na concentrations, although some xenolithic clinopyroxenes extend to higher Na
306 contents (Fig. 6A). The Floreana clinopyroxenes display a large range of Cr contents, ranging from
307 <0.05 wt% in the most evolved crystals to ~1.72 wt% in the more primitive crystals (Fig. 6B).

308 Clinopyroxene analyses are typically taken from the cores of crystals, but zoning was characterised by
309 a series of transects (and maps) on the xenolithic clinopyroxenes (see Supplementary Information).
310 Results indicate that the clinopyroxenes are unzoned with respect to most element (including MgO
311 and FeO), but some zoning is present in their Al₂O₃, TiO₂ and Cr₂O₃ contents. Specifically,
312 clinopyroxene crystal rims are typically characterised by elevated TiO₂, but lower Cr₂O₃ contents.

313 *5.3.2 Trace elements*

314 Our Floreana clinopyroxenes display a wide range of geochemical enrichment, with LREE to MREE
315 ratios varying from [La/Sm]_n ~0.2 to [La/Sm]_n ~3.1 (where n represents normalisation to the
316 primitive mantle composition of Sun and McDonough, 1989). Wehrlitic clinopyroxenes typically
317 have more enriched trace element ratios (such as [La/Sm]_n or [Ce/Y]_n) than clinopyroxenes from the
318 scoria samples (Fig. 7). Furthermore, melt [La/Sm]_n ratios calculated to be in equilibrium with
319 clinopyroxenes from the scoria and xenolith samples range from ~1 to ~15 (calculated using the major
320 element composition of the clinopyroxene at the location of LA-ICP-MS analysis and the elastic
321 strain model of Wood and Blundy (1997) at 1225°C and 700 MPa; Fig. 7B), significantly greater than
322 the range measured in Floreana whole-rock samples (~2–5, with a small number of outliers up to
323 ~7.5; Harpp et al. 2014a). Almost all of the xenolithic crystals, and a large proportion of the
324 clinopyroxenes separated from scoria deposits, are too enriched to be in equilibrium with the typical
325 composition of melts erupted on Floreana (Harpp et al., 2014a). In addition, there is a strong

326 correlation between the Na concentrations and highly/moderately incompatible trace element ratios of
327 the Floreana clinopyroxenes ($p < 10^{-3}$), such that crystals with enriched trace element signatures
328 typically contain a high jadeite component (Fig. 7A). Finally, the Floreana clinopyroxenes all contain
329 Eu anomalies ($Eu^* = Eu_n / \sqrt{Sm_n \times Gd_n}$) within analytical uncertainty of 1, and Sr anomalies ($Sr^* =$
330 $Sr_n / \sqrt{Pr_n \times Nd_n}$) that have a similar range to that observed in the erupted basalts (Harpp et al.,
331 2014a).

332 **6 MAGMA SYSTEM ARCHITECTURE BENEATH** 333 **ISLA FLOREANA**

334 **6.1 Mush crystallisation and textural equilibration**

335 Based on pyroxene trace element and radiogenic isotope ratios, Lyons et al. (2007) hypothesised that
336 gabbroic xenoliths in the Floreana lava and scoria deposits formed in an ancient (>1 -1.5 Ma)
337 magmatic system, compositionally similar to those currently beneath Cerro Azul and Sierra Negra
338 volcanoes in the western Galápagos. In contrast, wehrlite xenoliths preserve isotopic ratios similar to
339 more recent subaerial lavas on Floreana, suggesting that they are fragments of the present-day
340 magmatic system (Lyons et al., 2007).

341 Our wehrlitic xenoliths preserve an original poikilitic igneous texture (clinopyroxene oikocrysts
342 surrounding olivine chadacrysts) and display no evidence for the metamorphic breakdown of
343 plagioclase (e.g. pseudomorphs or relict cores) as hypothesised by Lyons et al. (2007). We suggest
344 that the clinopyroxene crystals in our wehrlitic xenoliths grew within an olivine-dominated cumulate
345 mush (i.e. interstitial growth of clinopyroxene oikocrysts; Wager et al., 1960). If clinopyroxene
346 growth is principally within a crystal-rich (i.e. relatively viscous and immobile) mush zone, this could
347 explain its relatively low abundance in Floreana lava and scoria deposits ($<5\%$ of separated crystals).
348 In contrast, plagioclase triple junctions in the gabbroic xenoliths have $\sim 120^\circ$ dihedral angles (Fig. 3A),
349 indicating a high degree of textural equilibration (Holness et al., 2019, 2005). Plagioclase textural
350 equilibrium, along with the two-pyroxene phase assemblage, suggests that the gabbroic xenoliths

351 represent magmatic cumulates which were stored at high temperatures (>900°C) on long timescales
352 (Holness et al., 2006). These petrographic observations are consistent with the gabbroic nodules
353 sampling an ancient magmatic system beneath Floreana (>1 Ma; Lyons et al., 2007).

354 **6.2 Mush disaggregation prior to eruption**

355 *6.2.1 Insights from olivine compositional heterogeneity*

356 Olivine crystals separated from the Floreana lava and scoria samples have a wide range of zoning
357 patterns, morphologies, and compositions (Fig. 2). The five olivine groups identified in the Floreana
358 samples have distinct morphologies and zoning patterns (see Section 2 above), suggesting chemically
359 heterogeneous magma storage (Holness et al., 2019). In particular, the most evolved crystals (Group
360 4; Fo~70–75) are in equilibrium with melts that are more evolved than the Floreana erupted basalts
361 (likely basaltic andesites). This is consistent with a recent study which identified highly evolved
362 (andesitic - dacitic) magmas beneath basaltic volcanoes in the western Galápagos Archipelago (Stock
363 et al., 2020).

364 As Fe-Mg interdiffusion in olivine is geologically fast (Chakraborty, 2010; Costa et al., 2020),
365 preservation of forsterite zoning in the Floreana olivine crystals suggests that multiple magma batches
366 interacted on relatively short pre-eruptive timescales. In Group 5 olivines, for example, four
367 compositional zones are preserved over ~100-200 µm (Fig. 2E and F). Whilst we do not have enough
368 Group 5 olivine crystals to calculate statistically robust timescales of pre-eruptive magma interactions
369 using diffusion chronometry, complex forsterite zoning over ~100 µm is estimated to last <3 yrs at the
370 approximate temperature of basaltic magma storage (~1225°C; using diffusion coefficients from
371 Chakraborty, 2010). Therefore, we suggest that the range of crystal morphologies and major element
372 compositions displayed by the Floreana olivines in lava and scoria deposits indicates mixing of
373 chemically heterogeneous magma storage regions over relatively short timescales prior to eruption.

374 The minor element chemistry of the olivine crystals allows us to investigate the crystallinity of these
375 chemically diverse magma storage regions. Olivine crystals in our Floreana lava and scoria deposits
376 have an unusually low, and large range of Ca concentrations (~250–2600 ppm compared with ~1500-
377 3000 ppm in the eastern Galápagos; Gleeson and Gibson, 2019; Fig. 5A). The lower end of the range

378 in Ca concentrations measured in the Floreana lava and scoria deposits overlaps with those observed
379 in cumulate xenoliths (wehrlites) and thus are unlikely to represent mantle olivines (Thompson and
380 Gibson, 2000). Previous studies have shown that the Ca concentration of magmatic olivine is sensitive
381 to several parameters, including: (i) the major element composition of the co-existing melt phase
382 (Herzberg, 2011); (ii) the H₂O content of the co-existing melt phase (Gavrilenko et al., 2016); and (iii)
383 the temperature of the system (Adams and Bishop, 1982; Köhler and Brey, 1990; Shejwalkar and
384 Coogan, 2013).

385 Variations in the Ca content of primary mantle melts are commonly hypothesised to result from the
386 presence of a lithologically heterogeneous mantle source (Herzberg, 2011; Sobolev et al., 2007;
387 Vidito et al., 2013). Specifically, melting of a pyroxene-rich mantle lithology is expected to produce
388 Ca-poor and Ni-rich melts which would go on to form Ca-poor, but Ni-rich, olivines. While the low
389 Ca contents of many of the Floreana olivines would therefore appear to indicate derivation from melts
390 of a pyroxenitic source lithology, the olivine Ni contents are relatively low (<3000 ppm), inconsistent
391 with this hypothesis (Fig. 5B; Gleeson and Gibson, 2019). As a result, if the low Ca contents of the
392 Floreana olivines represent equilibrium with low Ca melts, we require a different process to generate
393 these compositions. This process must reduce the Ca concentration of the melt phase (and co-existing
394 olivines), without simultaneously reducing the melt Mg# (as low Ca concentrations are observed
395 across the entire range of forsterite contents in the Floreana olivines; Fig. 5A).

396 Evidence for the origin of the low-Ca contents in the Floreana olivines from lava and scoria deposits
397 is present in the texture and composition of the wehrlitic xenoliths, which contain uniformly low-Ca
398 olivine crystals (<1000 ppm; Fig. 5A). The petrography of the wehrlitic xenoliths attests to
399 clinopyroxene growth within olivine-dominated mush regions. Clinopyroxene crystallisation within
400 this mush would extract CaO and MgO from the residual melt. However, in an olivine-rich mush, the
401 large reservoir of MgO contained within the cumulus olivine grains would buffer the residual melt at
402 a near-constant Mg# during clinopyroxene crystallisation (Meyer et al., 1989). In contrast, the CaO
403 concentration of the melt is not buffered and decreasing melt CaO contents, due to clinopyroxene
404 crystallisation, will cause the CaO concentration of cumulus olivine grains to decrease (as a result of

405 diffusive re-equilibration). Support for this interpretation comes from the anomalously low CaO
406 concentrations in the matrix glass of sample 17MMSG27.

407 Intercumulus clinopyroxene growth would also increase the H₂O concentration of the residual melt
408 phase, decreasing the partition coefficient of Ca into olivine (Gavrilenko et al., 2016). Therefore,
409 variable amounts of clinopyroxene crystallisation within an olivine-dominated mush, and subsequent
410 disaggregation of this mush by an ascending melt, could explain the range of Ca contents measured in
411 the Floreana olivines derived from lava and scoria deposits. Specifically, we suggest that: (i)
412 forsteritic olivine crystals (Fo>83) with Ca contents >1500 ppm are consistent with those expected
413 from fractional crystallisation of mantle-derived melts in a liquid-rich magma storage region (Fig. 5A;
414 Gleeson and Gibson, 2019); (ii) olivines with Ca contents <1000 ppm, overlapping with the wehrlitic
415 olivines, reflect equilibrium with Ca-poor interstitial melts; and (iii) olivine crystals with intermediate
416 Ca concentrations (1000 – 1500 ppm) are sourced from regions where clinopyroxene growth is less
417 extensive, or ongoing at the time of eruption. Thus, the olivine crystal cargo of the Floreana magmas
418 is predominantly derived from crystal-rich domains with only a small number of olivine crystals
419 displaying compositions that are consistent with fractional crystallisation in liquid-rich storage regions
420 (Ca >1500 ppm; Gleeson and Gibson, 2019).

421 It is an important to note, however, that the partitioning of Ca between co-existing olivine and
422 clinopyroxene has been hypothesised to be sensitive to temperature (such that less Ca enters the
423 olivine structure at lower temperature; Shejwalkar and Coogan, 2013). As a result, the heterogeneity
424 in the Ca content of the Floreana olivines could instead represent disaggregation of xenolithic material
425 that has undergone variable amounts of cooling. Both hypotheses presented here can recreate the
426 range of Ca contents observed in the Floreana olivines and, as the majority of olivine analyses from
427 the Floreana lava and scoria deposits have low Ca concentrations (<1000 ppm) that overlap with those
428 in xenolithic nodules, indicate that a large proportion of the erupted crystal cargo derives from
429 disaggregated, highly crystalline magma storage regions.

430 6.2.2 *Insights from clinopyroxene major element compositions*

431 The compositions of clinopyroxene crystals from the Floreana scoria also overlap with those in our
432 xenolith samples, supporting the hypothesis that some of the erupted crystals are derived from
433 disaggregated sub-volcanic mush (Fig. 6). We used hierarchical cluster analysis to subdivide our 567
434 clinopyroxene major element analyses from the Floreana scoria and xenolith samples and determine
435 the proportion of material that is derived from each xenolith lithology in the erupted crystal cargo
436 (cluster analysis was performed in Python 3.8 using the scikit-learn package of Pedregosa et al. 2011).
437 We find that our clinopyroxene analyses form three distinct clusters (Fig. 8):

- 438 - Cluster 1 clinopyroxenes are predominantly from the wehrlite and dunite xenoliths and
439 include 90% of our analyses from these samples. 39% of clinopyroxenes analysed from the
440 scoria samples also fall into this cluster.
- 441 - Cluster 2 clinopyroxenes include all analyses from the gabbroic xenoliths, and ~10% of
442 analyses from crystals separated from the scoria samples.
- 443 - Cluster 3 clinopyroxenes are dominated by analyses of the scoria derived clinopyroxenes
444 (~50% of analyses from the scoria separates). However, 10% of analyses from the wehrlite
445 and dunite xenoliths also fall into this cluster.

446 Of our 248 clinopyroxenes analyses from the Floreana scoria, approximately half are classified as
447 Cluster 3 and thus have major element compositions that do not show a clear chemical affinity to
448 either the wehrlite/dunite or gabbroic cumulates. Therefore, these crystals may represent autocrysts
449 (defined here as crystals that are genetically related to primary mantle melts beneath Floreana, but are
450 not influenced by secondary cumulate processes) that grew in liquid-rich magma storage regions. The
451 remainder of clinopyroxene analyses from the scoria are either compositionally analogous to those in
452 the wehrlite and dunite xenoliths (Cluster 1; 39%) or the gabbroic xenoliths (Cluster 2; 11%); we
453 interpret these as representing disaggregated sub-volcanic mush or wall rock. The high proportion of
454 the clinopyroxene crystal cargo that is derived from highly crystalline storage regions beneath
455 Floreana is consistent with our interpretation of olivine minor element concentrations.

456 **6.3 Reactive Porous Flow within a cumulate mush**

457 Whilst the olivine and clinopyroxene major and minor element concentrations show that a large
458 proportion of the erupted crystal cargo is derived from highly crystalline magma storage regions,
459 clinopyroxene trace element concentrations (and zoning) reveal the magmatic processes that operate
460 within these crystal-rich domains. The trace element composition of melts in equilibrium with our
461 clinopyroxene crystals are calculated using the model of Wood and Blundy (1997). The results
462 indicate that many of our clinopyroxene analyses have incompatible trace element ratios (e.g.
463 $[Ce/Y]_n$) which are more enriched than any erupted basalt from Floreana (Harpp et al., 2014a). In fact,
464 nearly all clinopyroxene analyses from our xenolith samples, and ~50% of clinopyroxene analyses
465 from the scoria samples, record trace element disequilibrium with the typical composition of the
466 Floreana basalts (Fig. 7 and 9). Over-enriched trace element signatures are characteristic of Cluster 1
467 clinopyroxenes (i.e. chemical affinity to the wehrlitic or dunitic xenoliths), whereas crystals that are
468 near trace element equilibrium with Floreana basalts typically have Cluster 3 major element
469 compositions (i.e. the autocryst cluster).

470 Petrographic observations and olivine minor element data indicate that the Floreana sub-volcanic
471 system is characterised by clinopyroxene crystallisation within an olivine-dominated mush. If the
472 clinopyroxene grew from trapped melt within an olivine-dominated mush, progressive crystallisation
473 would increase the concentration of highly incompatible trace elements (e.g. Ba, La, Ce) relative to
474 less incompatible trace-elements (e.g. Sm, Y) in the residual melt. A simple fractional crystallisation
475 model indicates that ~70% crystallisation is required to generate melt $[Ce/Y]_n$ ratios that are in
476 equilibrium with enriched clinopyroxenes from the scoria samples and even greater extents of
477 crystallisation (~80%) would be required to generate the extremely high $[Ce/Y]_n$ ratios in some of the
478 xenolithic clinopyroxenes (Fig. 9).

479 Such extensive fractional crystallisation would be expected to result in the saturation and
480 crystallisation of plagioclase and other accessory phases (e.g. apatite, magnetite/ilmenite, quartz),
481 which are observed in more evolved xenoliths from Rabida island in the central Galápagos (Holness
482 et al., 2019). However, these phases are absent in the Floreana xenoliths, indicating that either

483 infiltration of melts from a highly enriched mantle source component or a different magmatic process
484 within the cumulate mush is responsible for generating the anomalous trace element signatures of the
485 Floreana clinopyroxenes. Infiltration of mantle-derived melts that are more enriched than anything
486 observed in erupted basalts on Floreana is considered unlikely owing to the overlapping isotopic
487 composition of xenoliths and erupted lavas (Lyons et al., 2007), and the absence of a significant
488 correlation between trace element enrichment and radiogenic isotope compositions in the erupted
489 Floreana basalts (see Supplementary Information; Harpp et al., 2014a). As a result, a process other
490 than source heterogeneity must be responsible for generating the trace element variation in both the
491 Floreana xenoliths and erupted basalts.

492 One alternative mechanism that might be able to generate the observed trace element over-enrichment
493 is reactive porous flow. In this scenario, clinopyroxene is precipitated from ascending clinopyroxene-
494 saturated melts that continuously react with the existing, olivine-dominated crystal framework as the
495 system approaches equilibrium, and thus deviates from a simple fractional crystallisation trajectory
496 (Lissenberg and MacLeod, 2016). As a result, reactive porous flow in the olivine-dominated mush
497 beneath Floreana will likely result in substantial crystallisation of clinopyroxene, possibly at the
498 expense of pre-existing crystal phases, with little to no formation of olivine or saturation of minor
499 phases. Consequently, reactive porous flow can lead to enrichment of highly- to moderately-
500 incompatible trace elements in the resulting melt (Coogan et al., 2000; Gao et al., 2007; Lissenberg et
501 al., 2013; Lissenberg and MacLeod, 2016), and is consistent with the petrography of the Floreana
502 xenoliths. For example, major element maps of clinopyroxene crystals in the Floreana wehrlites show
503 that they are zoned, with Ti-rich rims (Fig. 10); equivalent zoning patterns have been attributed to
504 reactive porous flow in plutonic clinopyroxenes from the oceanic crust (e.g. Hess Deep; Lissenberg
505 and MacLeod, 2016). In addition, if pre-existing Cr-spinel was dissolved by the reacting melt, then
506 reactive porous flow could also explain the high Cr contents of clinopyroxene in our wehrlitic
507 xenoliths (Fig. 6; Lissenberg and MacLeod, 2016).

508 To test whether reactive porous flow of clinopyroxene saturated melts through an olivine-dominated
509 mush is consistent with the trace element compositions of melts calculated to be in equilibrium with
510 our Floreana clinopyroxenes, we use the zone refining model of Harris (1957; Fig. 9):

$$\frac{C_l}{C_l^o} = \frac{1}{D} - \left(\frac{1}{D} - 1\right)e^{-DI}$$

512 (eq. 1)

513 where D is the bulk partition coefficient; C_l^o and C_l are the initial and final concentration of that
514 element in the melt phase, respectively; and I is the 'equivalent volumes of solid processed by the
515 liquid' (Lissenberg and MacLeod, 2016). The model assumes continuous reaction of the percolating
516 melt front with the existing crystal framework, and has previously been employed to investigate
517 geochemical signatures in oceanic gabbros (Lissenberg and MacLeod, 2016). Results indicate that
518 reactive porous flow can produce melts with trace element compositions that are comparable with
519 those in equilibrium with our Floreana clinopyroxenes (i.e. $[\text{Ce}/\text{Y}]_n \sim 8-13$) using I values that are
520 similar to those invoked in other magmatic settings worldwide ($\sim 2-5$ compared to $\sim 4-8$ for the Hess
521 Deep; Lissenberg and MacLeod, 2016). Hence, reactive porous flow represents a realistic mechanism
522 for generating the geochemical diversity of Floreana clinopyroxenes, including the trace element
523 enriched crystals analysed in the wehrlitic nodules (Fig. 9).

524 In addition, detailed LA-ICP-MS transects of two clinopyroxene grains from the most enriched
525 wehrlitic xenolith analysed in this study (17MMSG02c) show clear trace element zoning (Fig. 11).
526 The core of the larger clinopyroxene crystal has low $[\text{Ce}]$ and $[\text{Ce}/\text{Y}]_n$ contents that are approximately
527 in equilibrium with Floreana basalts (Harpp et al. 2014a; Fig. 11a), whereas the mantle and rim of the
528 crystal is characterised by increasing $[\text{Ce}]$ and $[\text{Ce}/\text{Y}]_n$ contents. We interpret this as core
529 crystallisation from a melt with a trace element signature similar to that of erupted Floreana basalts
530 (Harpp et al., 2014a), followed by growth from a melt which became progressively enriched during
531 reactive porous flow (Fig. 11).

532 The mantle of the second, smaller xenolithic clinopyroxene shows a similar rim-ward increase in [Ce]
533 (interpreted as progressive melt enrichment during reactive porous flow). However, the [Ce] and
534 [Ce/Y]_n values of the crystal core are too high to be in equilibrium with erupted Floreana basalts (Fig.
535 11C). This is consistent with our spot analyses of clinopyroxene cores in other crystals and samples.
536 The high [Ce] and [Ce/Y]_n values measured in crystal cores cannot be explained by inward diffusion
537 of Ce, owing to significant differences in the diffusivities of Ce and Y and similar [Ce] and [Y]
538 zoning patterns in our two crystal transects (Fig. 11; Van Orman, 2001). Instead, we suggest that the
539 high apparent core [Ce] and [Ce/Y]_n contents in many of the Floreana clinopyroxenes record
540 crystallisation from melts that had already undergone geochemical enrichment via reactive porous
541 flow. However, we cannot discount that our apparent clinopyroxene cores are fragments of larger
542 oikocrysts that have been broken during mush disaggregation or sample crushing and, as a result, do
543 not represent the true core compositions of each crystal.

544 Nevertheless, our clinopyroxene major and trace element data, as well as petrographic observations of
545 the wehrlitic xenoliths, provide substantial evidence that reactive porous flow is an important
546 mechanism of melt migration and melt differentiation in highly crystalline magma storage regions
547 beneath Floreana. Although reactive porous flow has been identified as an important process in MOR
548 gabbros, this is the first study to identify reactive porous flow in an ocean island setting.

549 **6.4 Petrographic estimates of magma storage pressures**

550 Petrological and geophysical constraints on magma storage depths exist for several recently active
551 volcanoes in the western Galápagos Archipelago (Bagnardi et al., 2013; Case et al., 1973; Geist et al.,
552 1998; Stock et al., 2018; Vigouroux et al., 2008). However, in the absence of geophysical data (owing
553 to a paucity of recent eruptions), there are far fewer constraints on the structure of magma storage
554 regions in the eastern and south-eastern archipelago. To date, the only investigation of magma storage
555 depths beneath these volcanoes is by Geist et al. (1998), who undertook a visual comparison between
556 whole-rock lava compositions and the MORB olivine + plagioclase + augite + melt pseudoinvariant
557 point, parameterised by Grove et al. (1992). This approach is subject to substantial uncertainty, but the

558 authors suggest that the Floreana magmas consistently equilibrate at >5 kbar (typically >7 kbar) at a
559 depth >16 km, within the upper mantle.

560 We used three petrological barometers to provide improved constraints on magma storage depths
561 beneath Floreana. First, we applied the clinopyroxene-only barometer and thermometer of Putirka
562 (2008; equations 32b and 32d, respectively), in which pressure and temperature are solved iteratively
563 based solely on the clinopyroxene major element composition (primarily the jadeite component;
564 standard error of estimate [SEE] ± 310 MPa). Second, we applied the clinopyroxene-melt barometer of
565 Neave and Putirka (2017; equation 1), which uses the composition of a co-existing melt phase and the
566 proportion of the Jadeite component in clinopyroxene to calculate the pressure of crystallisation (SEE
567 = ± 140 MPa; pressure is solved iteratively with temperature using the clinopyroxene-melt
568 thermometer of Putirka, 2008; equation 33). Third, for the xenolithic nodules, we estimate the final
569 pressure and temperature of storage using the two-pyroxene thermobarometer of Putirka (2008;
570 equations 36 and 39; SEE = ± 280 MPa).

571 Taken at face value, initial application of the clinopyroxene-only barometer to all clinopyroxene
572 analyses from the scoria and xenolith samples gives a range of pressure estimates between ~ 450 MPa
573 and ~ 1800 MPa. However, reactive porous flow has a substantial influence on the compositions of the
574 Cluster 1 (and Cluster 2) clinopyroxenes, which may influence the barometric results. Specifically,
575 crystals that show evidence for reactive porous flow also have elevated Na concentrations, leading to
576 an anomalously high jadeite component and thus calculated pressure. This likely originates from the
577 presence of unusual melt compositions that fall outside the calibration range of the clinopyroxene-
578 only barometer owing to reactive melt migration, which is supported by the unusual glass
579 compositions in sample 17MMSG27 (Fig. 4). Therefore, we filter our dataset to remove crystals that
580 show a chemical signature indicative of reactive porous flow and only use Cluster 3 clinopyroxenes
581 that have trace element compositions in equilibrium with the Floreana basalts (using the whole-rock
582 data from Harpp et al. 2014) in our barometric calculations (n=78). Barometric results from this
583 filtered dataset indicate that crystallisation beneath Floreana occurs at a pressure of 766 ± 322 MPa

584 (2 σ of calculated pressures), which equates to a depth of 25.2 \pm 9.9 km (using the crustal density
585 estimate of Putirka (1997) and a mantle density estimate of 3300 kg/m³; Fig. 12).

586 Application of the Neave and Putirka (2017) clinopyroxene-melt barometer requires identification of
587 equilibrium clinopyroxene-liquid pairs. We achieve this using an automated melt-matching algorithm
588 (as in Winpenny and MacLennan, 2011, Neave and Putirka, 2017, Stock et al. 2018), with $K_D(\text{Fe-Mg})$,
589 diopside-hedenbergite, enstatite-ferrosillite and calcium Tschermak's equilibrium tests ($K_D(\text{Fe-Mg})$
590 within ± 0.03 other components within 2 SEE; Putirka, 1999, Putirka, 2008, Mollo et al., 2013). We
591 used the whole-rock data of Harpp et al. (2014a) and basaltic glass analyses from this study as
592 potential equilibrium liquids. Input crystal compositions were again filtered to remove analyses that
593 showed evidence of reactive porous flow (i.e. only Cluster 3 clinopyroxenes in trace element
594 equilibrium with the Floreana whole-rock were used). In total, 70 of the 78 input clinopyroxene
595 analyses returned at least one equilibrium match to either the basaltic glass or whole-rock
596 compositions. Where clinopyroxene compositions produced an equilibrium match with more than one
597 melt composition, an average melt composition was used in the barometric model. Results from this
598 barometer, coupled to the thermometer of Putirka (2008), indicate that magma crystallisation occurred
599 at 717 \pm 165 MPa (23.7 \pm 5.1 km) and 1224 \pm 33°C (Fig. 12).

600 Clinopyroxene-orthopyroxene thermobarometry records the final storage conditions of the cumulate
601 xenoliths, rather than the crystallisation conditions of clinopyroxene autocrysts (orthopyroxene is only
602 found as an intercumulus phase). Temperature and pressure estimates were only calculated from
603 orthopyroxene-clinopyroxene pairs in wehrlite and dunite xenoliths that passed the $K_D(\text{Fe-Mg})$
604 equilibrium test of Putirka (2008; 1.09 \pm 0.14). Results suggest that the cumulates were stored at
605 \sim 975–1100°C and 600–900 MPa, with a mean storage pressure of 712 \pm 200 MPa (23.7 \pm 6.4 km; Fig.
606 12).

607 The depths of magma storage calculated from our three petrological barometers show an excellent
608 agreement within the model uncertainties. These new data provide robust evidence that magma
609 storage beneath Floreana occurs below the Moho (\sim 16 km; Feighner and Richards, 1994), in the upper
610 mantle.

611 **7 IMPLICATIONS FOR MAGMATIC PLUMBING**
612 **SYSTEMS BENEATH LOW MELT FLUX OCEAN**
613 **ISLAND VOLCANOES**

614 Our new petrological and geochemical data show that magma storage beneath Floreana occurs in
615 mush-dominated regions of the upper mantle (Fig. 13). Mineral chemistry (such as low olivine Ca
616 concentrations and clinopyroxene major elements) reveal that a substantial portion of the erupted
617 crystal cargo is derived from disaggregated mush and wall rock material which has been entrained
618 into the ascending magmas. During ascent, magmas may entrain coherent nodules (xenoliths) as well
619 as disaggregated mush (Fig. 13). Coherent nodules represent areas of the magmatic system beneath
620 Floreana that have undergone cooling to temperatures <1100°C (compared to the clinopyroxene
621 crystallisation temperatures of ~1225°C) and may represent material from the border of the active
622 mush zone or older, almost completely solidified magma storage regions that are intersected during
623 magma ascent (Fig. 13).

624 Petrographic observations and clinopyroxene trace element chemistry from both the xenolith and
625 scoria samples reveal that clinopyroxene growth occurs via reactive porous flow in the mush-
626 dominated areas beneath Floreana. Reactive porous flow causes distinct trace element enrichment in
627 the percolating melt phase and crystallising clinopyroxene, which can explain the trace element
628 disequilibrium between the erupted Floreana basalts and their clinopyroxene cargo. Nevertheless, the
629 presence of some clinopyroxene crystals with major and trace element compositions in equilibrium
630 with erupted Floreana basalts indicates that at least some crystallisation occurs in liquid-rich sub-
631 volcanic storage regions, likely situated as localised melt pockets within the larger mush zone (Fig.
632 13).

633 Transport of melts modified by reactive porous flow into these melt pockets could impact the LREE
634 enriched signature of the resultant hybridised melts. This could help to explain the unique, concave up
635 REE signature of the Floreana basalts, which is not seen in other regions of the Galápagos
636 Archipelago (Harpp et al., 2014a). However, it is important to note that similar trace element
637 signatures are not observed in other, low melt-flux regions of the eastern Galapagos (such as San

638 Cristobal; Geist et al., 1986). As a result, we hypothesise that the unique REE pattern of the Floreana
639 basalts is primarily a source signature, likely associated with the highly radiogenic Pb and Sr isotope
640 signatures that characterise the Floreana basalts (Harpp et al., 2014a; Harpp and White, 2001).
641 Nevertheless, a few basalts on Floreana have trace element signatures that are far more enriched than
642 the majority of erupted basalts ($[La/Sm]_n$ up to 7.5), but are isotopically indistinguishable (Harpp et
643 al., 2014a); we therefore suggest that these basalts contain an anomalously large contribution of melts
644 that have undergone geochemical modification due to reactive porous flow.

645 Our results indicate substantial differences in the architecture of the magmatic systems beneath
646 Floreana and the frequently active shield volcanoes in the western Galápagos Archipelago. For
647 example, previous petrological and geophysical studies have identified that western Galápagos
648 magmatic systems are characterised by crustal magma storage, often with a large storage region in the
649 mid-to-lower crust (~7 km depth) and a smaller storage region at shallow levels, within the volcanic
650 edifice (~1 km depth; Geist et al. 1998; Bagnardi et al. 2013; Bagnardi and Hooper, 2018; Stock et al.,
651 2018; Fig 12). In contrast, our barometric data indicate that magmas beneath Floreana ascend directly
652 from the upper mantle and undergo no detectable crustal storage. In addition, although mush-rich
653 regions have been inferred beneath the western Galápagos shield volcanoes (based on whole-rock data
654 and the presence of gabbroic glomerocrysts; Chadwick et al., 2011; Geist et al., 1995, 2014; Stock et
655 al., 2018), magmatic differentiation appears to be driven by simple fractional crystallisation and
656 mixing of chemically diverse magmas (Geist et al., 1995; Naumann and Geist, 1999; Stock et al.,
657 2020).

658 One major factor that differentiates Floreana from shield volcanoes in the western archipelago is the
659 flux of magma into the lithosphere, which is evidenced by the large variations in the volumetric
660 eruption rate on Floreana and the western shields (Harpp et al., 2014a; Harpp and Geist, 2018; Kurz et
661 al., 2014). Hence, we suggest that the greater pressure of magma storage and prevalence of reactive
662 porous flow beneath Floreana, relative to volcanoes in the western archipelago, are related to the
663 substantially lower flux of magma into the lithosphere from the underlying mantle source (and thus
664 the thermal structure of the lithosphere). For example, the magma flux entering the lithosphere

665 beneath Wolf volcano (northern Isabela) has been substantially greater than that beneath Floreana for
666 several 100,000s of years (Geist et al., 2005). The high magma flux beneath Wolf maintains the
667 average temperature of the mid-to-lower crust at $\sim 1125^{\circ}\text{C}$ ($\Delta T \sim 22^{\circ}\text{C}$), with only small-scale thermal
668 and compositional heterogeneities present in the sub-volcanic plumbing system (Geist et al., 2014,
669 2005; Stock et al., 2020, 2018). In contrast, the flux of magma entering the magmatic system beneath
670 Floreana is much lower and the temperature of the mid-crust is likely to be significantly cooler than
671 the lowest temperature recorded by the Floreana xenoliths (that is, $\ll 900^{\circ}\text{C}$; Fig. 12). As the flux of
672 magma (and heat) from the mantle is insufficient to maintain an elevated crustal geotherm beneath
673 Floreana, magmas that stall in the crust are likely to rapidly crystallise, increase their viscosity, and
674 become uneruptable. Therefore, eruptions must be fed by melts ascending from much deeper storage
675 regions ($\sim 700\text{-}750$ MPa) where melts can persist over long time periods.

676 Our results have global implications for the architecture and dynamics of magma storage regions
677 beneath ocean island volcanoes worldwide. The observed difference in magma storage depths beneath
678 high and low melt flux volcanic systems in the Galapagos Archipelago is mirrored in a global
679 compilation of barometric data from ocean island volcanoes (Famin et al., 2009; Geist et al., 1998;
680 Hammer et al., 2016; Hartley et al., 2018; Klügel et al., 2015; Poland et al., 2015; Stock et al., 2018;
681 Zanon et al., 2020; Zanon and Pimentel, 2015). Using the average repose period between eruptions at
682 a particular basaltic volcanic centre as a proxy for the flux of magma entering the lithosphere from the
683 underlying mantle (Global Volcanism Program, 2013), Figure 14 shows that the most frequently
684 active volcanic centres (such as, Kīlauea, Hawai'i, and Piton de la Fournaise, Réunion) are
685 characterised by persistent magma storage in the mid to upper crust (Famin et al., 2009; Poland et al.,
686 2015). In contrast, less active centres located above low buoyancy flux plumes (e.g. El Hierro, Canary
687 Islands) and/or peripheral to the main zone of plume upwelling (e.g. Haleakalā, Hawai'i) are
688 characterised by longer repose periods and correspondingly greater magma storage pressures
689 (Hammer et al., 2016; Klügel et al., 2015; Zanon and Pimentel, 2015). In fact, although secondary
690 crustal magma staging can occur (Klügel et al., 2015), the main zone of magma storage beneath ocean
691 island volcanoes with repose periods >50 years is typically in the lithospheric mantle, below the base

692 of the crust (Longpre et al., 2014; Taracsák et al., 2019; Zanon et al., 2020). Hence, we speculate that
693 the flux of magma from the underlying mantle source has a first-order control on the depth of magma
694 storage beneath ocean island volcanoes and, correspondingly, high-pressure magma storage – as
695 observed beneath Floreana – is characteristic of low melt flux ocean island volcanoes globally.

696 **8 CONCLUSIONS**

697 Petrographic and geochemical analyses of lava, scoria and xenolith samples from Floreana in the
698 south-eastern Galápagos Archipelago provide new insights into the architecture and dynamics of
699 magma storage beneath low melt flux ocean island volcanoes. Comparison of olivine and
700 clinopyroxene major, minor and trace element contents between our different sample types reveal that
701 a substantial portion of the erupted crystal cargo is derived from mush-dominated magma storage
702 regions beneath Floreana. Mineral textures, highly enriched clinopyroxene trace element signatures
703 and trace element zoning in the xenoliths reveals that reactive porous flow is an important process of
704 chemical differentiation and melt transport within these mush-dominated regions. Mixing between
705 melts that have been geochemically enriched by reactive porous flow and those in overlying liquid-
706 rich storage regions could contribute to the anomalous, concave-up REE signature of the Floreana
707 basalts, which is absent in other parts of the Galápagos Archipelago where reactive porous flow has
708 not been identified.

709 Application of independent petrological barometers to crystals in Floreana scoria and xenolith
710 samples indicates that magmas are stored in the upper mantle ($\sim 23.7 \pm 5.1$ km). Floreana is in a distal
711 location to the Galápagos plume where the melt flux entering the lithosphere is low; the depth of
712 magma storage beneath Floreana contrasts with more proximal, higher melt flux volcanoes in the
713 western archipelago where magmas are stored in the crust (Geist et al., 1998; Stock et al., 2018).
714 Comparing our new data with ocean island volcanoes globally (e.g. Hawai'i, Iceland and the Canary
715 Islands) reveals that the Galápagos is not unique and that magma storage is ubiquitously shallower in
716 proximal magmatic systems above high buoyancy flux plumes than in off-axis systems, or above low
717 buoyancy flux plumes. We therefore suggest that the flux of mantle-derived magma entering the

718 lithosphere imparts a first-order control on the depth of magma storage beneath ocean island
719 volcanoes.

720 **ACKNOWLEDGEMENTS**

721 This study was supported by a NERC (Natural Environmental Research Council) Research Training
722 Student Grant (NE/L002507/1) awarded to M.L.M.G as well as NERC grant awarded to S.A.G
723 RG57434. M. J. S. was supported by a Charles Darwin and Galápagos Islands Junior Research
724 Fellowship at Christ's College, Cambridge. We are grateful to Iris Buisman and Jason Day for their
725 help with electron microprobe and laser-ablation inductively-coupled mass spectrometry analysis,
726 respectively. We also thank Margaret Hartley and John Maclennan for their comments on an early
727 version of this manuscript, as well as Dennis Geist and two anonymous reviewers for their helpful
728 comments that greatly improved this manuscript.

729 **REFERENCES**

- 730 Adams, G.E., Bishop, F.C., 1982. Experimental investigation of CaMg exchange between olivine,
731 orthopyroxene, and clinopyroxene: potential for geobarometry. *Earth Planet. Sci. Lett.* 57,
732 241–250. [https://doi.org/10.1016/0012-821X\(82\)90188-1](https://doi.org/10.1016/0012-821X(82)90188-1)
- 733 Allan, J.F., Simkin, T., 2000. Fernandina Volcano's evolved, well-mixed basalts: Mineralogical and
734 petrological constraints on the nature of the Galapagos plume. *J. Geophys. Res. Solid Earth*
735 105, 6017–6041. <https://doi.org/10.1029/1999JB900417>
- 736 Amelung, F., Jónsson, S., Zebker, H., Segall, P., 2000. Widespread uplift and 'trapdoor' faulting on
737 Galápagos volcanoes observed with radar interferometry. *Nature* 407, 993–996.
738 <https://doi.org/10.1038/35039604>
- 739 Asimow, P.D., Langmuir, C.H., 2003. The importance of water to oceanic mantle melting regimes.
740 *Nature* 421, 815–820. <https://doi.org/10.1038/nature01429>
- 741 Bagnardi, M., Amelung, F., Poland, M.P., 2013. A new model for the growth of basaltic shields based
742 on deformation of Fernandina volcano, Galápagos Islands. *Earth Planet. Sci. Lett.* 377–378,
743 358–366. <https://doi.org/10.1016/j.epsl.2013.07.016>
- 744 Bailey, K., 1976. Potassium-Argon Ages from the Galapagos Islands. *Science* 192, 465–467.
745 <https://doi.org/10.1126/science.192.4238.465>
- 746 Bernard, B., Stock, M.J., Coppola, D., Hidalgo, S., Bagnardi, M., Gibson, S., Hernandez, S., Ramón, P.,
747 Gleeson, M., 2019. Chronology and phenomenology of the 1982 and 2015 Wolf volcano
748 eruptions, Galápagos Archipelago. *J. Volcanol. Geotherm. Res.* 374, 26–38.
749 <https://doi.org/10.1016/j.jvolgeores.2019.02.013>
- 750 Bow, C.S., Geist, D.J., 1992. Geology and petrology of Floreana Island, Galapagos Archipelago,
751 Ecuador. *J. Volcanol. Geotherm. Res.* 52, 83–105. [https://doi.org/10.1016/0377-0273\(92\)90134-Y](https://doi.org/10.1016/0377-0273(92)90134-Y)
- 752
- 753 Case, J.E., Ryland, S.L., Simkin, T., Howard, K.A., 1973. Gravitational Evidence for a Low-Density Mass
754 beneath the Galapagos Islands. *Science* 181, 1040–1042.
755 <https://doi.org/10.1126/science.181.4104.1040>
- 756 Chadwick, W.W., Howard, K.A., 1991. The pattern of circumferential and radial eruptive fissures on
757 the volcanoes of Fernandina and Isabela islands, Galapagos. *Bull. Volcanol.* 53, 259–275.
758 <https://doi.org/10.1007/BF00414523>
- 759 Chadwick, W.W., Jónsson, S., Geist, D.J., Poland, M., Johnson, D.J., Batt, S., Harpp, K.S., Ruiz, A.,
760 2011. The May 2005 eruption of Fernandina volcano, Galápagos: The first circumferential

- 761 dike intrusion observed by GPS and InSAR. *Bull. Volcanol.* 73, 679–697.
762 <https://doi.org/10.1007/s00445-010-0433-0>
- 763 Chakraborty, S., 2010. Diffusion Coefficients in Olivine, Wadsleyite and Ringwoodite. *Rev. Mineral.*
764 *Geochem.* 72, 603–639. <https://doi.org/10.2138/rmg.2010.72.13>
- 765 Clague, D.A., Denlinger, R.P., 1994. Role of olivine cumulates in destabilizing the flanks of Hawaiian
766 volcanoes. *Bull. Volcanol.* 56, 425–434. <https://doi.org/10.1007/BF00302824>
- 767 Cleary, Z., Schwartz, D.M., Mittelstaedt, E., Harpp, K., 2020. Dynamic Magma Storage at Near-Ridge
768 Hot Spots: Evidence From New Galápagos Gravity Data. *Geochem. Geophys. Geosystems* 21.
769 <https://doi.org/10.1029/2019GC008722>
- 770 Coogan, L.A., Saunders, A.D., Kempton, P.D., Norry, M.J., 2000. Evidence from oceanic gabbros for
771 porous melt migration within a crystal mush beneath the Mid-Atlantic Ridge. *Geochem.*
772 *Geophys. Geosystems* 1, n/a-n/a. <https://doi.org/10.1029/2000GC000072>
- 773 Costa, F., Shea, T., Ubide, T., 2020. Diffusion chronometry and the timescales of magmatic processes.
774 *Nat. Rev. Earth Environ.* <https://doi.org/10.1038/s43017-020-0038-x>
- 775 Davidge, L., Ebinger, C., Ruiz, M., Tepp, G., Amelung, F., Geist, D., Coté, D., Anzieta, J., 2017.
776 Seismicity patterns during a period of inflation at Sierra Negra volcano, Galápagos Ocean
777 Island Chain. *Earth Planet. Sci. Lett.* 462, 169–179.
778 <https://doi.org/10.1016/j.epsl.2016.12.021>
- 779 Donaldson, C.H., 1976. An experimental investigation of olivine morphology. *Contrib. Mineral.*
780 *Petrol.* 57, 187–213. <https://doi.org/10.1007/BF00405225>
- 781 Famin, V., Welsch, B., Okumura, S., Bachèlery, P., Nakashima, S., 2009. Three differentiation stages
782 of a single magma at Piton de la Fournaise volcano (Reunion hot spot). *Geochem. Geophys.*
783 *Geosystems* 10, n/a-n/a. <https://doi.org/10.1029/2008GC002015>
- 784 Feighner, M.A., Richards, M.A., 1994. Lithospheric structure and compensation mechanisms of the
785 Galápagos Archipelago. *J. Geophys. Res.* 99, 6711. <https://doi.org/10.1029/93JB03360>
- 786 Gao, Y., Hoefs, J., Hellebrand, E., von der Handt, A., Snow, J.E., 2007. Trace element zoning in
787 pyroxenes from ODP Hole 735B gabbros: diffusive exchange or synkinematic crystal
788 fractionation? *Contrib. Mineral. Petrol.* 153, 429–442. [https://doi.org/10.1007/s00410-006-](https://doi.org/10.1007/s00410-006-0158-4)
789 [0158-4](https://doi.org/10.1007/s00410-006-0158-4)
- 790 Gavrilenko, M., Herzberg, C., Vidito, C., Carr, M.J., Tenner, T., Ozerov, A., 2016. A Calcium-in-Olivine
791 Geohygrometer and its Application to Subduction Zone Magmatism. *J. Petrol.* 57, 1811–
792 1832. <https://doi.org/10.1093/petrology/egw062>
- 793 Geist, D., Howard, K.A., Larson, P., 1995. The Generation of Oceanic Rhyolites by Crystal
794 Fractionation: the Basalt-Rhyolite Association at Volc n Alcedo, Gal pagos Archipelago. *J.*
795 *Petrol.* 36, 965–982. <https://doi.org/10.1093/petrology/36.4.965>
- 796 Geist, D., Naumann, T., Larson, P., 1998. Evolution of Galapagos Magmas: Mantle and Crustal
797 Fractionation without Assimilation. *J. Petrol.* 39, 953–971.
798 <https://doi.org/10.1093/petroj/39.5.953>
- 799 Geist, D., White, W.M., Albarede, F., Harpp, K., Reynolds, R., Blichert-Toft, J., Kurz, M.D., 2002.
800 Volcanic evolution in the Galápagos: The dissected shield of Volcan Ecuador. *Geochem.*
801 *Geophys. Geosystems* 3, 1 of 32–32 32. <https://doi.org/10.1029/2002GC000355>
- 802 Geist, D.J., Bergantz, G., Chadwick, W.W., 2014. Galápagos Magma Chambers, in: Harpp, K.S.,
803 Mittelstaedt, E., d'Ozouville, N., Graham, D.W. (Eds.), *Geophysical Monograph Series*. John
804 Wiley & Sons, Inc, Hoboken, New Jersey, pp. 55–69.
805 <https://doi.org/10.1002/9781118852538.ch5>
- 806 Geist, D.J., Fornari, D.J., Kurz, M.D., Harpp, K.S., Adam Soule, S., Perfit, M.R., Koleszar, A.M., 2006.
807 Submarine Fernandina: Magmatism at the leading edge of the Galápagos hot spot.
808 *Geochem. Geophys. Geosystems* 7, n/a-n/a. <https://doi.org/10.1029/2006GC001290>
- 809 Geist, D.J., McBIRNEY, A.R., Duncan, R.A., 1986. Geology and petrogenesis of lavas from San
810 Cristobal Island, Galapagos Archipelago. *Geol. Soc. Am. Bull.* 97, 555.
811 [https://doi.org/10.1130/0016-7606\(1986\)97<555:GAPOLF>2.0.CO;2](https://doi.org/10.1130/0016-7606(1986)97<555:GAPOLF>2.0.CO;2)

- 812 Geist, D.J., Naumann, T.R., Standish, J.J., Kurz, M.D., Harpp, K.S., White, W.M., Fornari, D.J., 2005.
813 Wolf Volcano, Galápagos Archipelago: Melting and Magmatic Evolution at the Margins of a
814 Mantle Plume. *J. Petrol.* 46, 2197–2224. <https://doi.org/10.1093/petrology/egi052>
- 815 Geist, D.J., White, W.M., McBirney, A.R., 1988. Plume-asthenosphere mixing beneath the Galapagos
816 archipelago. *Nature* 333, 657–660. <https://doi.org/10.1038/333657a0>
- 817 Gibson, S.A., Dale, C.W., Geist, D.J., Day, J.A., Brüggmann, G., Harpp, K.S., 2016. The influence of melt
818 flux and crustal processing on Re–Os isotope systematics of ocean island basalts: Constraints
819 from Galápagos. *Earth Planet. Sci. Lett.* 449, 345–359.
820 <https://doi.org/10.1016/j.epsl.2016.05.021>
- 821 Gibson, S.A., Geist, D., 2010. Geochemical and geophysical estimates of lithospheric thickness
822 variation beneath Galápagos. *Earth Planet. Sci. Lett.* 300, 275–286.
823 <https://doi.org/10.1016/j.epsl.2010.10.002>
- 824 Gibson, S.A., Geist, D.G., Day, J.A., Dale, C.W., 2012. Short wavelength heterogeneity in the
825 Galápagos plume: Evidence from compositionally diverse basalts on Isla Santiago. *Geochem.*
826 *Geophys. Geosystems* 13. <https://doi.org/10.1029/2012GC004244>
- 827 Gleeson, M.L.M., Gibson, S.A., 2019. Crustal controls on apparent mantle pyroxenite signals in
828 ocean-island basalts. *Geology*. <https://doi.org/10.1130/G45759.1>
- 829 Gleeson, M.L.M., Gibson, S.A., Williams, H.M., 2020. Novel insights from Fe-isotopes into the
830 lithological heterogeneity of Ocean Island Basalts and plume-influenced MORBs. *Earth*
831 *Planet. Sci. Lett.* 535, 116114. <https://doi.org/10.1016/j.epsl.2020.116114>
- 832 Global Volcanism Program, 2013. *Volcanoes of the World*, v. 4.9.0 (04 Jun 2020). Venzke, E (ed.).
833 Smithsonian Institution. Downloaded 24th Aug (2020).
- 834 Grove, T.L., Kinzler, R.J., Bryan, W.B., 1992. Fractionation of Mid-Ocean Ridge Basalt (MORB), in:
835 Morgan, J.P., Blackman, D.K., Sinton, J.M. (Eds.), *Geophysical Monograph Series*. American
836 Geophysical Union, Washington, D. C., pp. 281–310. <https://doi.org/10.1029/GM071p0281>
- 837 Hammer, J., Jacob, S., Welsch, B., Hellebrand, E., Sinton, J., 2016. Clinopyroxene in postshield
838 Haleakala ankaramite: 1. Efficacy of thermobarometry. *Contrib. Mineral. Petrol.* 171, 7.
839 <https://doi.org/10.1007/s00410-015-1212-x>
- 840 Harpp, K.S., Geist, D.J., 2018. The Evolution of Galápagos Volcanoes: An Alternative Perspective.
841 *Front. Earth Sci.* 6. <https://doi.org/10.3389/feart.2018.00050>
- 842 Harpp, K.S., Geist, D.J., Koleszar, A.M., Christensen, B., Lyons, J., Sabga, M., Rollins, N., 2014a. The
843 Geology and Geochemistry of Isla Floreana, Galápagos: A Different Type of Late-Stage Ocean
844 Island Volcanism, in: Harpp, K.S., Mittelstaedt, E., d’Ozouville, N., Graham, D.W. (Eds.),
845 *Geophysical Monograph Series*. John Wiley & Sons, Inc, Hoboken, New Jersey, pp. 71–117.
846 <https://doi.org/10.1002/9781118852538.ch6>
- 847 Harpp, K.S., White, W.M., 2001. Tracing a mantle plume: Isotopic and trace element variations of
848 Galápagos seamounts. *Geochem. Geophys. Geosystems* 2, n/a-n/a.
849 <https://doi.org/10.1029/2000GC000137>
- 850 Harpp, K.S., Wirth, K.R., Teasdale, R., Blair, S., Reed, L., Barr, J., Pistiner, J., Korich, D., 2014b. Plume-
851 Ridge Interaction in the Galápagos: Perspectives from Wolf, Darwin, and Genovesa Islands,
852 in: Harpp, K.S., Mittelstaedt, E., d’Ozouville, N., Graham, D.W. (Eds.), *Geophysical*
853 *Monograph Series*. John Wiley & Sons, Inc, Hoboken, New Jersey, pp. 285–334.
854 <https://doi.org/10.1002/9781118852538.ch15>
- 855 Harris, P.G., 1957. Zone refining and the origin of potassic basalts. *Geochim. Cosmochim. Acta* 12,
856 195–208. [https://doi.org/10.1016/0016-7037\(57\)90032-7](https://doi.org/10.1016/0016-7037(57)90032-7)
- 857 Hartley, M.E., Bali, E., Maclennan, J., Neave, D.A., Halldórsson, S.A., 2018. Melt inclusion constraints
858 on petrogenesis of the 2014–2015 Holuhraun eruption, Iceland. *Contrib. Mineral. Petrol.*
859 173. <https://doi.org/10.1007/s00410-017-1435-0>
- 860 Herzberg, C., 2011. Identification of Source Lithology in the Hawaiian and Canary Islands:
861 Implications for Origins. *J. Petrol.* 52, 113–146. <https://doi.org/10.1093/petrology/egq075>

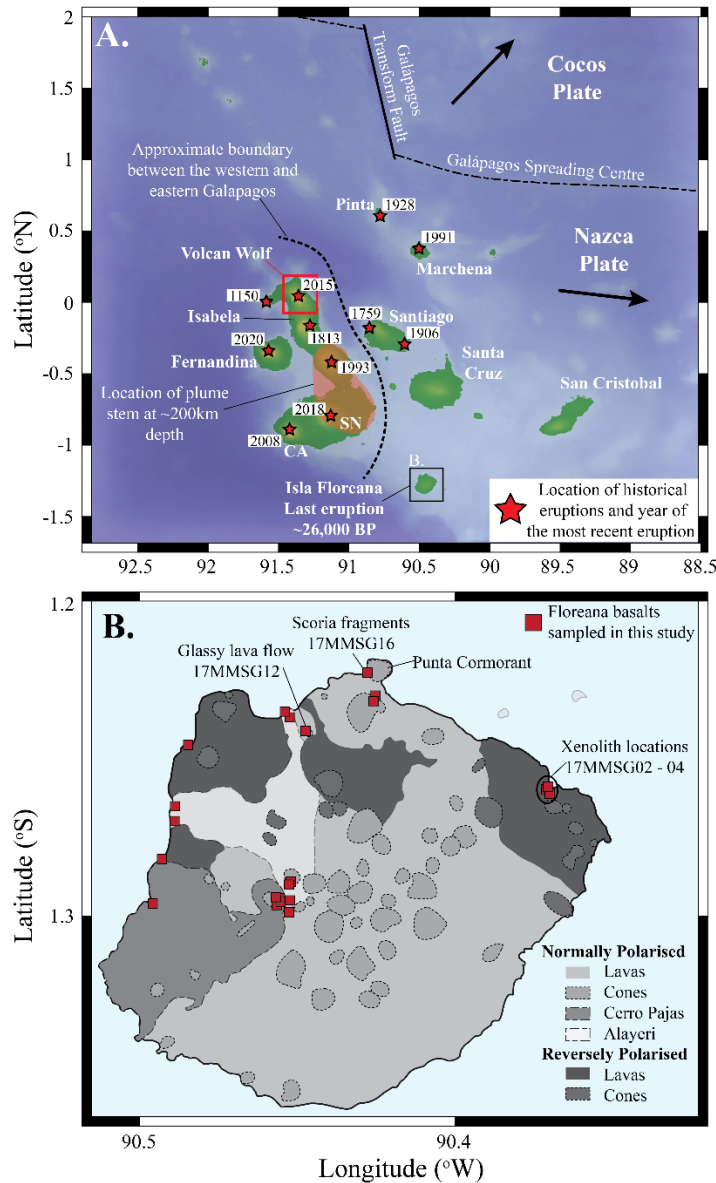
- 862 Hinton, R.W., 1999. NIST SRM 610, 611 and SRM 612, 613 Multi-Element Glasses: Constraints from
863 Element Abundance Ratios Measured by Microprobe Techniques. *Geostand. Geoanalytical*
864 *Res.* 23, 197–207. <https://doi.org/10.1111/j.1751-908X.1999.tb00574.x>
- 865 Holness, M.B., Cheadle, M.J., McKENZIE, D., 2005. On the Use of Changes in Dihedral Angle to
866 Decode Late-stage Textural Evolution in Cumulates. *J. Petrol.* 46, 1565–1583.
867 <https://doi.org/10.1093/petrology/egi026>
- 868 Holness, M.B., Nielsen, T.F.D., Tegner, C., 2006. Textural Maturity of Cumulates: a Record of
869 Chamber Filling, Liquidus Assemblage, Cooling Rate and Large-scale Convection in Mafic
870 Layered Intrusions. *J. Petrol.* 48, 141–157. <https://doi.org/10.1093/petrology/egl057>
- 871 Holness, M.B., Stock, M.J., Geist, D., 2019. Magma chambers versus mush zones: constraining the
872 architecture of sub-volcanic plumbing systems from microstructural analysis of crystalline
873 enclaves. *Philos. Trans. R. Soc. Math. Phys. Eng. Sci.* 377, 20180006.
874 <https://doi.org/10.1098/rsta.2018.0006>
- 875 Jackson, M.G., Konter, J.G., Becker, T.W., 2017. Primordial helium entrained by the hottest mantle
876 plumes. *Nature* 542, 340–343. <https://doi.org/10.1038/nature21023>
- 877 Jarosewich, E., Nelen, J.A., Norberg, J.A., 1980. Reference Samples for Electron Microprobe
878 Analysis*. *Geostand. Geoanalytical Res.* 4, 43–47. <https://doi.org/10.1111/j.1751-908X.1980.tb00273.x>
- 880 Jochum, K.P., Weis, U., Schwager, B., Stoll, B., Wilson, S.A., Haug, G.H., Andreae, M.O., Enzweiler, J.,
881 2016. Reference Values Following ISO Guidelines for Frequently Requested Rock Reference
882 Materials. *Geostand. Geoanalytical Res.* 40, 333–350. <https://doi.org/10.1111/j.1751-908X.2015.00392.x>
- 884 Kilbride, B.M., Edmonds, M., Biggs, J., 2016. Observing eruptions of gas-rich compressible magmas
885 from space. *Nat. Commun.* 7, 13744. <https://doi.org/10.1038/ncomms13744>
- 886 Klügel, A., Longpré, M.-A., García-Cañada, L., Stix, J., 2015. Deep intrusions, lateral magma transport
887 and related uplift at ocean island volcanoes. *Earth Planet. Sci. Lett.* 431, 140–149.
888 <https://doi.org/10.1016/j.epsl.2015.09.031>
- 889 Köhler, T.P., Brey, G.P., 1990. Calcium exchange between olivine and clinopyroxene calibrated as a
890 geothermobarometer for natural peridotites from 2 to 60 kb with applications. *Geochim.*
891 *Cosmochim. Acta* 54, 2375–2388. [https://doi.org/10.1016/0016-7037\(90\)90226-B](https://doi.org/10.1016/0016-7037(90)90226-B)
- 892 Kurz, M.D., Rowland, S.K., Curtice, J., Saal, A.E., Naumann, T., 2014. Eruption Rates for Fernandina
893 Volcano: A New Chronology at the Galápagos Hotspot Center, in: Harpp, K.S., Mittelstaedt,
894 E., d'Ozouville, N., Graham, D.W. (Eds.), *Geophysical Monograph Series*. John Wiley & Sons,
895 Inc, Hoboken, New Jersey, pp. 41–54. <https://doi.org/10.1002/9781118852538.ch4>
- 896 Lissenberg, C.J., MacLeod, C.J., 2016. A Reactive Porous Flow Control on Mid-ocean Ridge Magmatic
897 Evolution. *J. Petrol.* 57, 2195–2220. <https://doi.org/10.1093/petrology/egw074>
- 898 Lissenberg, C.J., MacLeod, C.J., Howard, K.A., Godard, M., 2013. Pervasive reactive melt migration
899 through fast-spreading lower oceanic crust (Hess Deep, equatorial Pacific Ocean). *Earth*
900 *Planet. Sci. Lett.* 361, 436–447. <https://doi.org/10.1016/j.epsl.2012.11.012>
- 901 Longpre, M.-A., Klugel, A., Diehl, A., Stix, J., 2014. Mixing in mantle magma reservoirs prior to and
902 during the 2011-2012 eruption at El Hierro, Canary Islands. *Geology* 42, 315–318.
903 <https://doi.org/10.1130/G35165.1>
- 904 Lyons, J., Geist, D., Harpp, K., Diefenbach, B., Olin, P., Vervoort, J., 2007. Crustal growth by magmatic
905 overplating in the Galápagos. *Geology* 35, 511. <https://doi.org/10.1130/G23044A.1>
- 906 Mahr, J., Harpp, K S, Kurz, M D, Geist, D, Bercovici, H., Pimentel, R., Cleary, Z., 2016. Rejuvenescent
907 Volcanism on San Cristóbal Island, Galápagos: A Late" Plumer". AGU Fall Abstr.
- 908 Matzen, A.K., Baker, M.B., Beckett, J.R., Stolper, E.M., 2011. Fe–Mg Partitioning between Olivine and
909 High-magnesian Melts and the Nature of Hawaiian Parental Liquids. *J. Petrol.* 52, 1243–1263.
910 <https://doi.org/10.1093/petrology/egq089>

- 911 Matzen, A.K., Baker, M.B., Beckett, J.R., Wood, B.J., Stolper, E.M., 2017a. The effect of liquid
912 composition on the partitioning of Ni between olivine and silicate melt. *Contrib. Mineral.*
913 *Petrol.* 172. <https://doi.org/10.1007/s00410-016-1319-8>
- 914 Matzen, A.K., Wood, B.J., Baker, M.B., Stolper, E.M., 2017b. The roles of pyroxenite and peridotite in
915 the mantle sources of oceanic basalts. *Nat. Geosci.* 10, 530–535.
916 <https://doi.org/10.1038/ngeo2968>
- 917 Meyer, P.S., Dick, H.J.B., Thompson, G., 1989. Cumulate gabbros from the Southwest Indian Ridge,
918 54°S–7°E: implications for magmatic processes at a slow spreading ridge. *Contrib.*
919 *Mineral. Petrol.* 103, 44–63. <https://doi.org/10.1007/BF00371364>
- 920 Mollo, S., Putirka, K., Misiti, V., Soligo, M., Scarlato, P., 2013. A new test for equilibrium based on
921 clinopyroxene–melt pairs: Clues on the solidification temperatures of Etnean alkaline melts
922 at post-eruptive conditions. *Chem. Geol.* 352, 92–100.
923 <https://doi.org/10.1016/j.chemgeo.2013.05.026>
- 924 Naumann, T., Geist, D., 2000. Physical volcanology and structural development of Cerro Azul
925 Volcano, Isabela Island, Galápagos: implications for the development of Galápagos-type
926 shield volcanoes. *Bull. Volcanol.* 61, 497–514. <https://doi.org/10.1007/s004450050001>
- 927 Naumann, T.R., Geist, D.J., 1999. Generation of alkalic basalt by crystal fractionation of tholeiitic
928 magma. *Geology* 27, 423. [https://doi.org/10.1130/0091-
929 7613\(1999\)027<0423:GOABBC>2.3.CO;2](https://doi.org/10.1130/0091-7613(1999)027<0423:GOABBC>2.3.CO;2)
- 930 Neal, C.A., Brantley, S.R., Antolik, L., Babb, J.L., Burgess, M., Calles, K., Cappos, M., Chang, J.C.,
931 Conway, S., Desmither, L., Dotray, P., Elias, T., Fukunaga, P., Fuke, S., Johanson, I.A.,
932 Kamibayashi, K., Kauahikaua, J., Lee, R.L., Pekalib, S., Miklius, A., Million, W., Moniz, C.J.,
933 Nadeau, P.A., Okubo, P., Parcheta, C., Patrick, M.R., Shiro, B., Swanson, D.A., Tollett, W.,
934 Trusdell, F., Younger, E.F., Zoeller, M.H., Montgomery-Brown, E.K., Anderson, K.R., Poland,
935 M.P., Ball, J.L., Bard, J., Coombs, M., Dietterich, H.R., Kern, C., Thelen, W.A., Cervelli, P.F.,
936 Orr, T., Houghton, B.F., Gansecki, C., Hazlett, R., Lundgren, P., Diefenbach, A.K., Lerner, A.H.,
937 Waite, G., Kelly, P., Clor, L., Werner, C., Mulliken, K., Fisher, G., Damby, D., 2019. The 2018
938 rift eruption and summit collapse of Kīlauea Volcano. *Science* 363, 367–374.
939 <https://doi.org/10.1126/science.aav7046>
- 940 Neave, D.A., Namur, O., Shorttle, O., Holtz, F., 2019. Magmatic evolution biases basaltic records of
941 mantle chemistry towards melts from recycled sources. *Earth Planet. Sci. Lett.* 520, 199–211.
942 <https://doi.org/10.1016/j.epsl.2019.06.003>
- 943 Neave, D.A., Putirka, K.D., 2017. A new clinopyroxene-liquid barometer, and implications for magma
944 storage pressures under Icelandic rift zones. *Am. Mineral.* 102, 777–794.
945 <https://doi.org/10.2138/am-2017-5968>
- 946 Park, J., Morgan, J.K., Zelt, C.A., Okubo, P.G., Peters, L., Benesh, N., 2007. Comparative velocity
947 structure of active Hawaiian volcanoes from 3-D onshore–offshore seismic tomography.
948 *Earth Planet. Sci. Lett.* 259, 500–516. <https://doi.org/10.1016/j.epsl.2007.05.008>
- 949 Pedregosa, F., Varoquaux, G., Gramfort, A., Michel, V., Thirion, B., Grisel, O., Blondel, M.,
950 Prettenhofer, P., Weiss, R., Dubourg, V., Vanderplas, J., Passos, A., Cournapeau, D., Brucher,
951 M., Perrot, M., Duchesnay, E., 2011. Scikit-learn: Machine Learning in Python. *J. Mach.*
952 *Learn. Res.* 12, 2825–2830.
- 953 Peterson, M.E., Kelley, K.A., Cottrell, E., Saal, A.E., Kurz, M.D., 2015. The Oxidation State of Fe in
954 Glasses from the Galapagos Archipelago: Variable Oxygen Fugacity as a Function of Mantle
955 Source. *AGU Fall Abstr.*
- 956 Peterson, M.E., Saal, A.E., Kurz, M.D., Hauri, E.H., Blusztajn, J.S., Harpp, K.S., Werner, R., Geist, D.J.,
957 2017. Submarine Basaltic Glasses from the Galapagos Archipelago: Determining the Volatile
958 Budget of the Mantle Plume. *J. Petrol.* 58, 1419–1450.
959 <https://doi.org/10.1093/petrology/egx059>

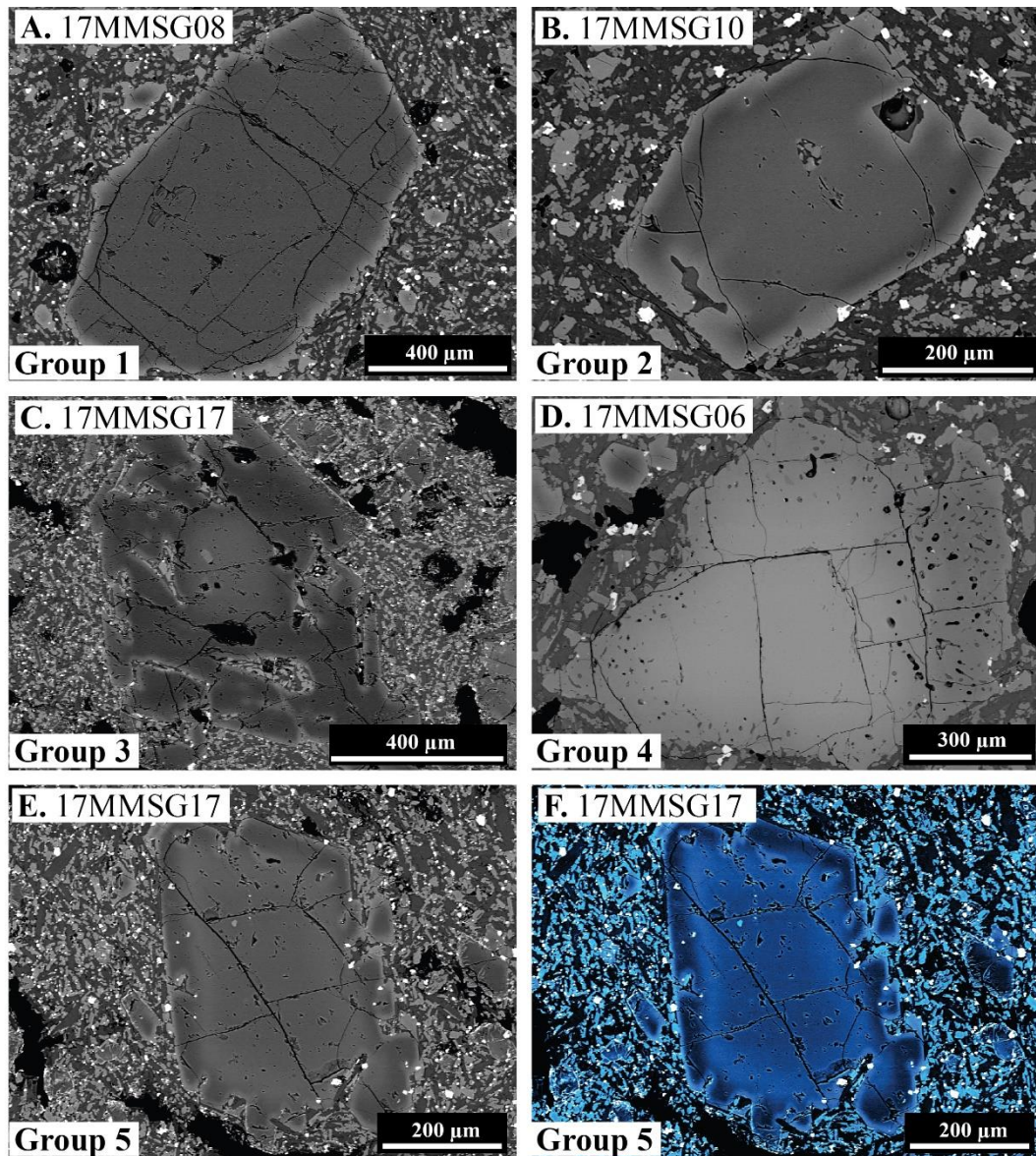
- 960 Pietruszka, A.J., Heaton, D.E., Marske, J.P., Garcia, M.O., 2015. Two magma bodies beneath the
961 summit of Kīlauea Volcano unveiled by isotopically distinct melt deliveries from the mantle.
962 *Earth Planet. Sci. Lett.* 413, 90–100. <https://doi.org/10.1016/j.epsl.2014.12.040>
- 963 Poland, M.P., Miklius, A., Montgomery-Brown, E.K., 2015. Magma supply, storage, and transport at
964 shield stage Hawaiian volcanoes, in: *Characteristics of Hawaiian Volcanoes*.
- 965 Putirka, K., 1999. Clinopyroxene + liquid equilibria to 100 kbar and 2450 K. *Contrib. Mineral. Petrol.*
966 135, 151–163. <https://doi.org/10.1007/s004100050503>
- 967 Putirka, K., 1997. Magma transport at Hawaii: Inferences based on igneous thermobarometry 4.
- 968 Putirka, K.D., 2008. Thermometers and Barometers for Volcanic Systems. *Rev. Mineral. Geochem.*
969 69, 61–120. <https://doi.org/10.2138/rmg.2008.69.3>
- 970 Roeder, P.L., Emslie, R.F., 1970. Olivine-liquid equilibrium. *Contrib. Mineral. Petrol.* 29, 275–289.
971 <https://doi.org/10.1007/BF00371276>
- 972 Shejwalkar, A., Coogan, L.A., 2013. Experimental calibration of the roles of temperature and
973 composition in the Ca-in-olivine geothermometer at 0.1MPa. *Lithos* 177, 54–60.
974 <https://doi.org/10.1016/j.lithos.2013.06.013>
- 975 Sides, I., Edmonds, M., MacLennan, J., Houghton, B.F., Swanson, D.A., Steele-MacInnis, M.J., 2014.
976 Magma mixing and high fountaining during the 1959 Kīlauea Iki eruption, Hawai‘i. *Earth*
977 *Planet. Sci. Lett.* 400, 102–112. <https://doi.org/10.1016/j.epsl.2014.05.024>
- 978 Sobolev, A.V., Hofmann, A.W., Kuzmin, D.V., Yaxley, G.M., Arndt, N.T., Chung, S.-L., Danyushevsky,
979 L.V., Elliott, T., Frey, F.A., Garcia, M.O., Gurenko, A.A., Kamenetsky, V.S., Kerr, A.C.,
980 Krivolutsкая, N.A., Matvienkov, V.V., Nikogosian, I.K., Rocholl, A., Sigurdsson, I.A.,
981 Sushchevskaya, N.M., Teklay, M., 2007. The Amount of Recycled Crust in Sources of Mantle-
982 Derived Melts 316, 7.
- 983 Stock, M.J., Bagnardi, M., Neave, D.A., MacLennan, J., Bernard, B., Buisman, I., Gleeson, M.L.M.,
984 Geist, D., 2018. Integrated Petrological and Geophysical Constraints on Magma System
985 Architecture in the Western Galápagos Archipelago: Insights From Wolf Volcano. *Geochem.*
986 *Geophys. Geosystems* 19, 4722–4743. <https://doi.org/10.1029/2018GC007936>
- 987 Stock, M.J., Geist, D., Neave, D.A., Gleeson, M.L.M., Bernard, B., Howard, K.A., Buisman, I.,
988 MacLennan, J., 2020. Cryptic evolved melts beneath monotonous basaltic shield volcanoes in
989 the Galápagos Archipelago. *Nat. Commun.* 11, 3767. <https://doi.org/10.1038/s41467-020-17590-x>
- 991 Sun, S. -s., McDonough, W.F., 1989. Chemical and isotopic systematics of oceanic basalts:
992 implications for mantle composition and processes. *Geol. Soc. Lond. Spec. Publ.* 42, 313–
993 345. <https://doi.org/10.1144/GSL.SP.1989.042.01.19>
- 994 Taracsák, Z., Hartley, M.E., Burgess, R., Edmonds, M., Iddon, F., Longpré, M.-A., 2019. High fluxes of
995 deep volatiles from ocean island volcanoes: Insights from El Hierro, Canary Islands. *Geochim.*
996 *Cosmochim. Acta* 258, 19–36. <https://doi.org/10.1016/j.gca.2019.05.020>
- 997 Thompson, R., 1987. Phase-equilibria constraints on the genesis and magmatic evolution of oceanic
998 basalts. *Earth-Sci. Rev.* 24, 161–210. [https://doi.org/10.1016/0012-8252\(87\)90023-7](https://doi.org/10.1016/0012-8252(87)90023-7)
- 999 Thompson, R.N., Gibson, S.A., 2000. Transient high temperatures in mantle plume heads inferred
1000 from magnesian olivines in Phanerozoic picrites. *Nature* 407, 502–506.
1001 <https://doi.org/10.1038/35035058>
- 1002 Vidito, C., Herzberg, C., Gazel, E., Geist, D., Harpp, K., 2013. Lithological structure of the Galápagos
1003 Plume: Lithological Structure Galpagos Plume. *Geochem. Geophys. Geosystems* 14, 4214–
1004 4240. <https://doi.org/10.1002/ggge.20270>
- 1005 Vigouroux, N., Williams-Jones, G., Chadwick, W., Geist, D., Ruiz, A., Johnson, D., 2008. 4D gravity
1006 changes associated with the 2005 eruption of Sierra Negra volcano, Galápagos. *GEOPHYSICS*
1007 73, WA29–WA35. <https://doi.org/10.1190/1.2987399>
- 1008 Villagómez, D.R., Toomey, D.R., Geist, D.J., Hooft, E.E.E., Solomon, S.C., 2014. Mantle flow and
1009 multistage melting beneath the Galápagos hotspot revealed by seismic imaging. *Nat. Geosci.*
1010 7, 151–156. <https://doi.org/10.1038/ngeo2062>

- 1011 Wager, L.R., Brown, G.M., Wadsworth, W.J., 1960. Types of Igneous Cumulates. *J. Petrol.* 1, 73–85.
1012 <https://doi.org/10.1093/petrology/1.1.73>
- 1013 Ward, J.H., 1963. Hierarchical Grouping to Optimize an Objective Function. *J. Am. Stat. Assoc.* 58,
1014 236–244. <https://doi.org/10.1080/01621459.1963.10500845>
- 1015 Welsch, B., Hammer, J., Hellebrand, E., 2014. Phosphorus zoning reveals dendritic architecture of
1016 olivine. *Geology* 42, 867–870. <https://doi.org/10.1130/G35691.1>
- 1017 White, W.M., McBirney, A.R., Duncan, R.A., 1993. Petrology and geochemistry of the Galápagos
1018 Islands: Portrait of a pathological mantle plume. *J. Geophys. Res. Solid Earth* 98, 19533–
1019 19563. <https://doi.org/10.1029/93JB02018>
- 1020 Wieser, P.E., Edmonds, M., Maclennan, J., Jenner, F.E., Kunz, B.E., 2019. Crystal scavenging from
1021 mush piles recorded by melt inclusions. *Nat. Commun.* 10, 5797.
1022 <https://doi.org/10.1038/s41467-019-13518-2>
- 1023 Wieser, P.E., Edmonds, M., Maclennan, J., Wheeler, J., 2020. Microstructural constraints on
1024 magmatic mushes under Kīlauea Volcano, Hawai‘i. *Nat. Commun.* 11, 14.
1025 <https://doi.org/10.1038/s41467-019-13635-y>
- 1026 Winpenny, B., Maclennan, J., 2011. A Partial Record of Mixing of Mantle Melts Preserved in Icelandic
1027 Phenocrysts. *J. Petrol.* 52, 1791–1812. <https://doi.org/10.1093/petrology/egr031>
- 1028 Wood, B.J., Blundy, J.D., 1997. A predictive model for rare earth element partitioning between
1029 clinopyroxene and anhydrous silicate melt. *Contrib. Mineral. Petrol.* 129, 166–181.
1030 <https://doi.org/10.1007/s004100050330>
- 1031 Zanon, V., Pimentel, A., 2015. Spatio-temporal constraints on magma storage and ascent conditions
1032 in a transtensional tectonic setting: The case of the Terceira Island (Azores). *Am. Mineral.*
1033 100, 795–805. <https://doi.org/10.2138/am-2015-4936>
- 1034 Zanon, V., Pimentel, A., Auxerre, M., Marchini, G., Stuart, F.M., 2020. Unravelling the magma feeding
1035 system of a young basaltic oceanic volcano. *Lithos* 352–353, 105325.
1036 <https://doi.org/10.1016/j.lithos.2019.105325>
1037

FIGURES

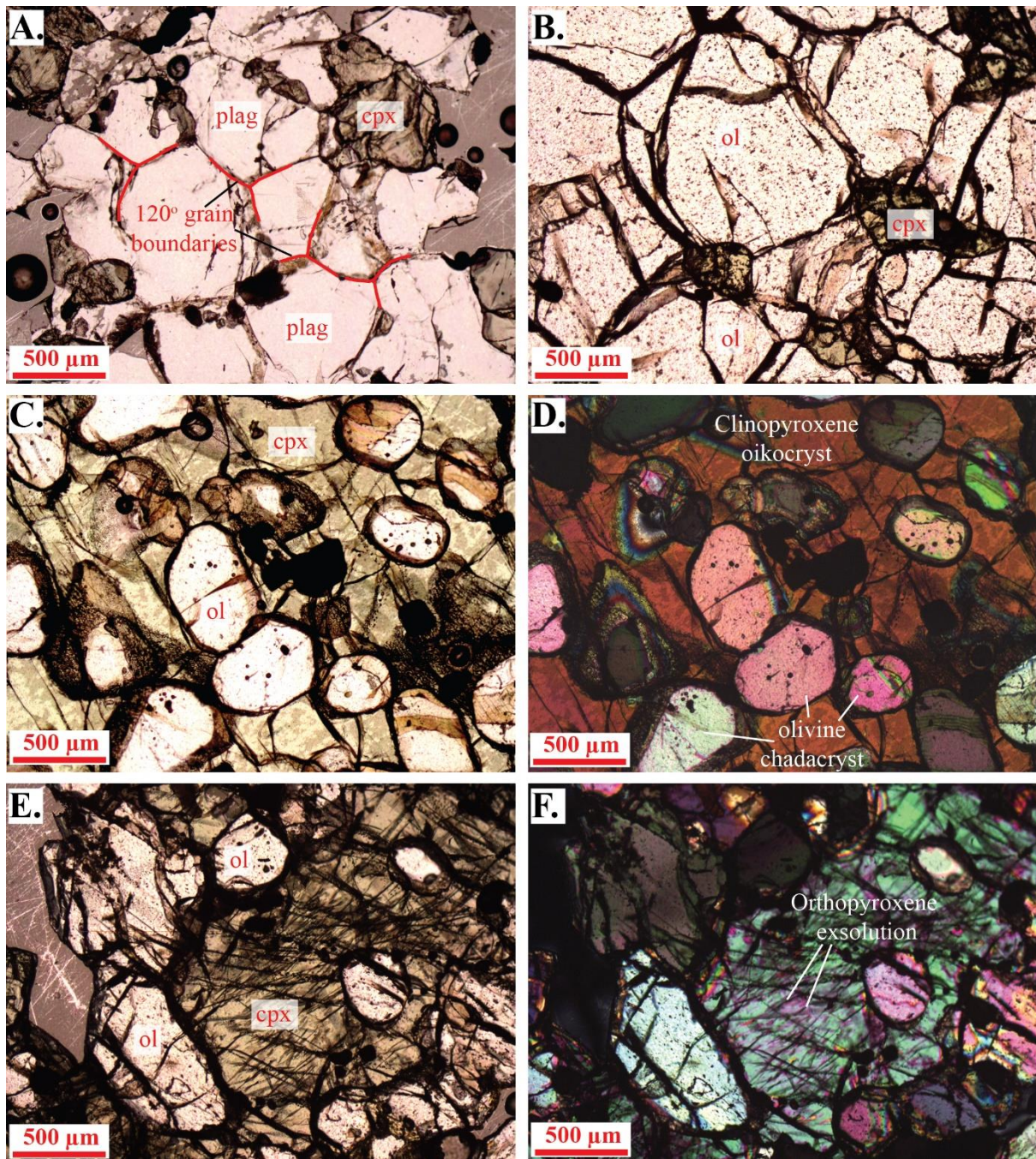


1040 **Figure 1 - A.** Regional map of the Galápagos Archipelago highlighting the location of Isla Floreana,
1041 Cerro Azul (CA), Sierra Negra (SN) and Wolf volcanoes. Dates show the most recent eruptions at
1042 historically active volcanic centres. Black arrows show the direction of plate motion for the Nazca and
1043 Cocos tectonic plates. **B.** Geological map of Floreana adapted from Harpp et al. (2014a). Dashed lines
1044 delineate monogenetic scoria cones. Normally and reversely polarised lava flows are shown along
1045 with the largest (Cerro Pajas) and most recent (Alayeri; ~26,000 years) eruptions on the island.



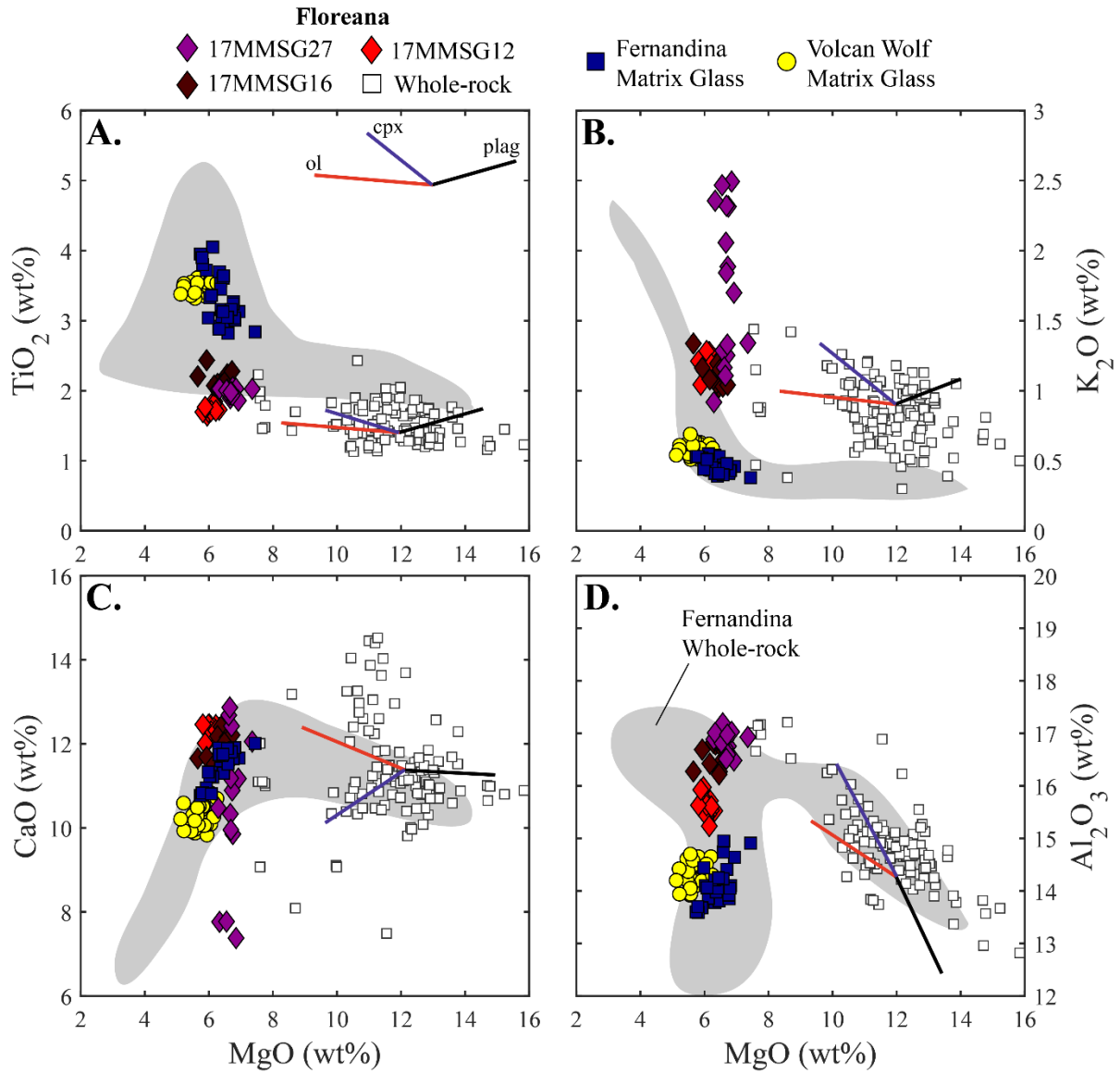
1046

1047 **Figure 2** – Backscatter Electron images. **A.** Group 1 olivines – euhedral to subhedral crystal
1048 morphologies with large, unzoned, crystal cores and narrow, normally-zoned rims. **B.** Group 2
1049 olivines – subhedral to euhedral crystals with clear, reverse-zoning profiles. **C.** Group 3 olivines –
1050 skeletal crystals with high forsterite overgrowths on low forsterite cores. **D.** Group 4 olivines –
1051 anhedral crystals with sieved textured, reverse zoned rims. **E.** (greyscale) and **F.** (false colour) Group
1052 5 olivines – crystals preserve at least 4 composition zones over ~100-200 μm. False colour image (**F.**)
1053 is used to highlight the compositional zoning of the Group 5 olivine, with the intensity of the blue
1054 colour associated with the Fo composition of the crystal (darker = higher Fo).



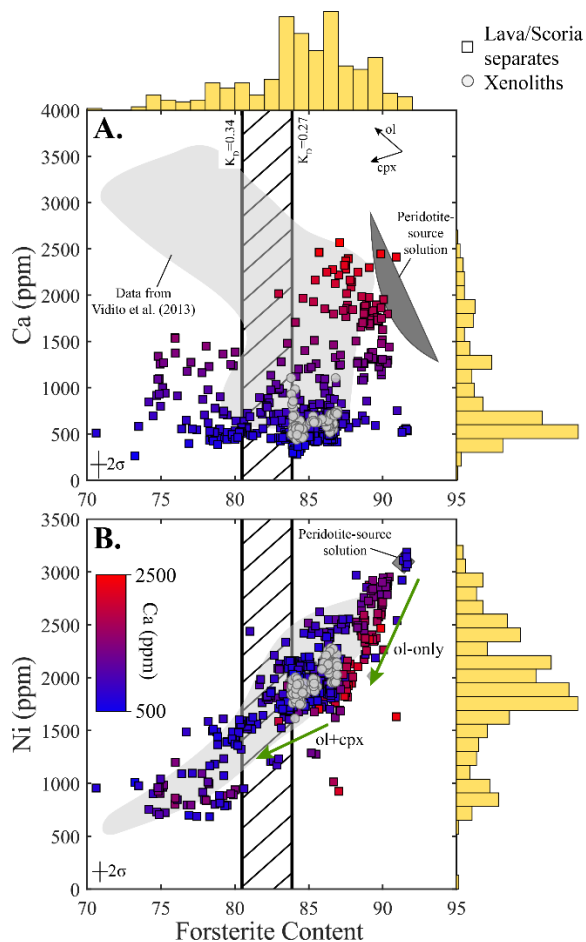
1055

1056 **Figure 3** - Plane Polarised Light (A. – C. and E.) and Crossed Polarised Light (D., F.) images of
1057 Floreana xenoliths. **A.** – gabbroic xenolith (17MMSG04b), highlighting near 120° grain boundaries at
1058 monomineralic plagioclase (plag) triple junctions. **B.** – dunitic xenolith (17MMSG04c) with
1059 intercumulus clinopyroxene (cpx). **C.** and **D.** – wehrlitic xenolith (17MMSG02c) showing a large
1060 clinopyroxene oikocryst surrounding olivine (ol) chadacrysts. **E.** and **F.** – wehrlitic xenolith (sample
1061 17MMSG03a) showing olivine chadacrysts within a clinopyroxene oikocryst. Orthopyroxene
1062 exsolution lamellae are visible within the clinopyroxene.



1063

1064 **Figure 4** – Major element compositions of matrix glasses (this study) and whole-rocks (Harpp et al.,
1065 2014a) from Floreana, as well as glasses from Fernandina (Peterson et al., 2017) and Wolf volcano
1066 (Stock et al., 2018) in the western Galápagos Archipelago. Lines show trajectories of liquid
1067 compositional evolution for olivine (ol; red), clinopyroxene (cpx; blue) and plagioclase (plag; black)
1068 crystallisation. The grey field shows whole-rock data from Isla Fernandina in the western Galápagos
1069 (Allan and Simkin, 2000; Geist et al., 2006). The 2 σ precision of our matrix glass analyses is smaller
1070 than the symbol size.



1071

1072

Figure 5 – Major and minor element compositions of olivine crystals from the Isla Floreana basalts.

1073

A. Fo vs. Ca and **B** Fo vs. Ni in Galápagos olivine crystals displaying analyses from our lava/scoria

1074

separates and xenolith samples, as well as a compilation of available olivine data from Floreana

1075

(Vidito et al. 2013). Our lava/scoria analyses are coloured according to their Ca concentration. The

1076

histograms above and to the right of the plots show the data distributions (excluding *in situ* analyses

1077

of xenolithic olivines). Peridotite source solutions are taken from Herzberg (2011) and Matzen et al.

1078

(2017a). Black arrows in **A.** show the trajectory of crystal compositional evolution during olivine (ol)

1079

and clinopyroxene (cpx) crystallisation (taken from Gleeson and Gibson, 2019). The green lines in **B.**

1080

show the trajectories of crystal compositional evolution during olivine only and olivine +

1081

clinopyroxene fractional crystallisation (from Gleeson and Gibson, 2019). The vertical black lines

1082

show the forsterite compositions of crystals calculated to be in equilibrium with the matrix glass

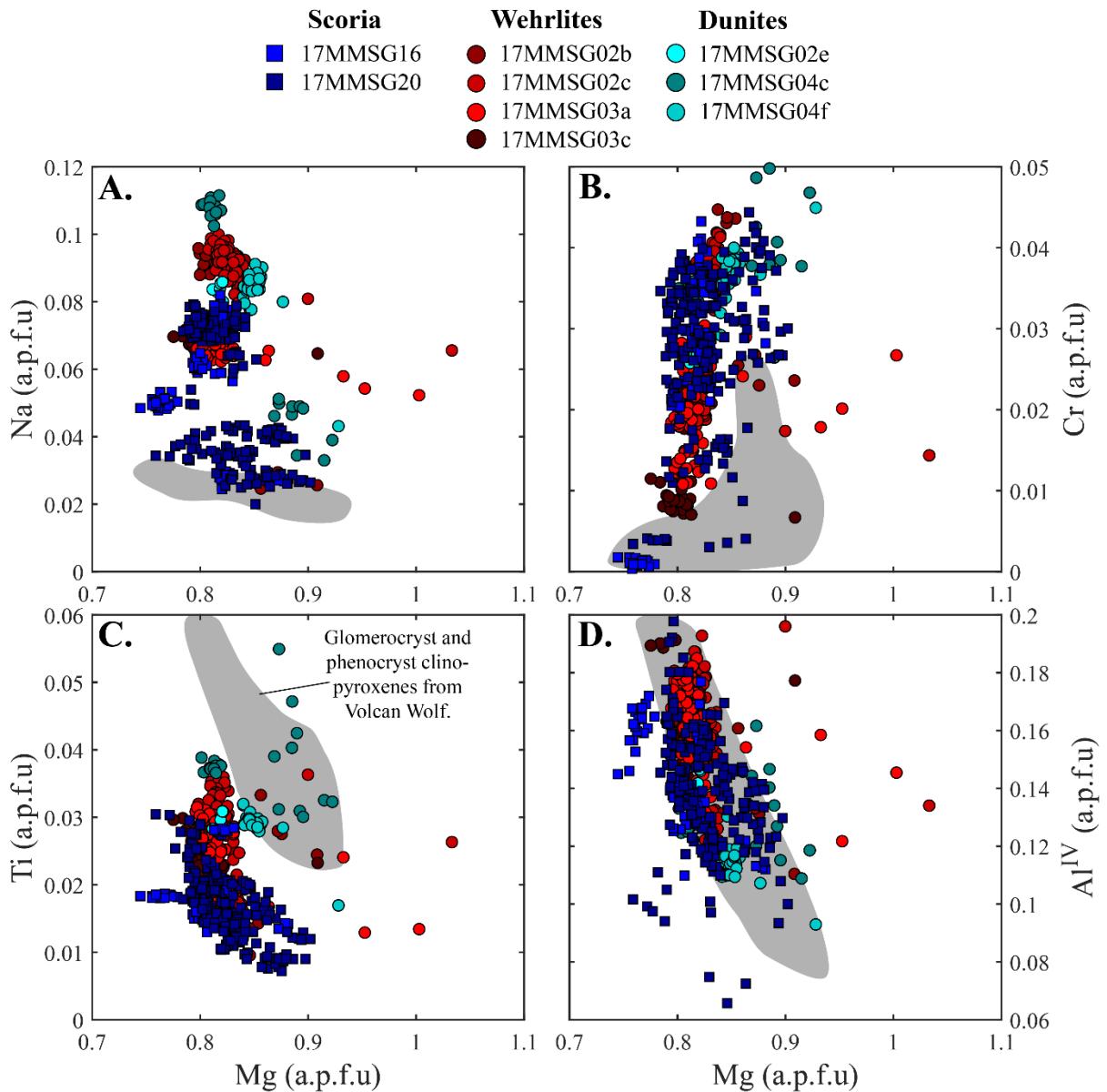
1083

composition of tephra sample 17MMSG16 ($K_d = 0.27 - 0.34$ after Matzen et al. 2011, and Roeder and

1084

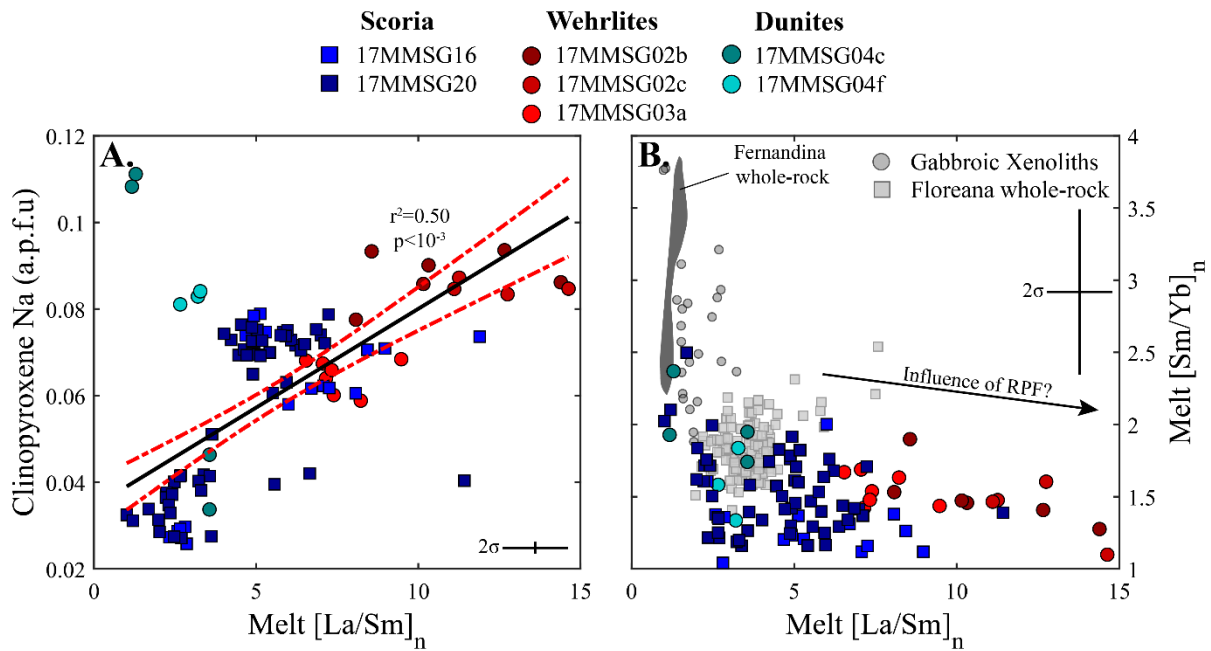
Emslie 1970).

Floreana Clinopyroxenes



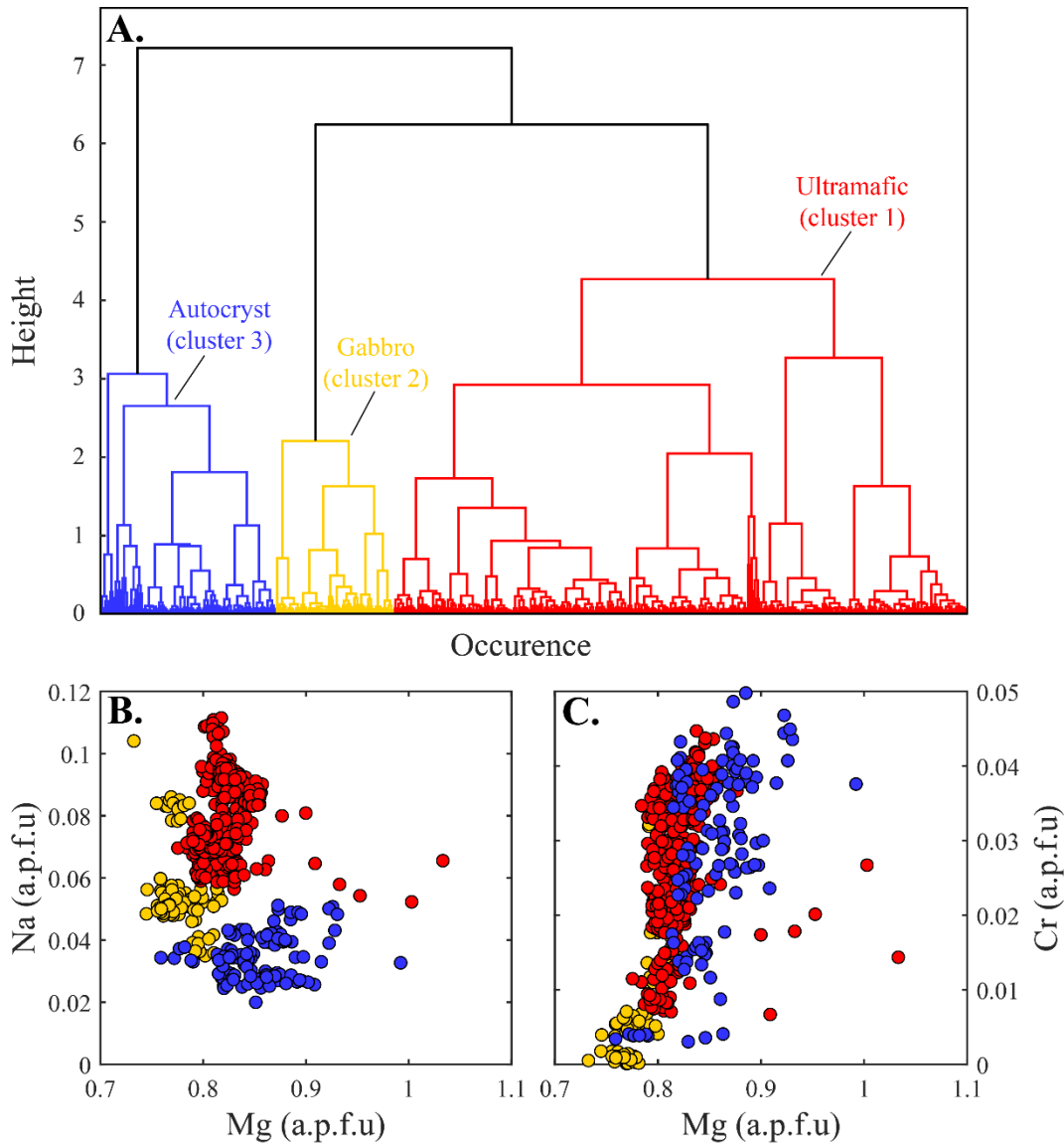
1085

1086 **Figure 6** – Major element composition of Floreana clinopyroxenes from our scoria, wehrlite and
1087 dunite samples. Data is shown as atoms per formula unit (a.p.f.u) on the basis of 6 oxygens. The grey
1088 field shows the compositions of clinopyroxenes from Wolf volcano in the western Galápagos
1089 Archipelago (from Stock et al. 2018). The 2 σ precision of our clinopyroxene analyses is smaller than
1090 the symbol size.



1091

1092 **Figure 7** – Trace element composition of the Floreana clinopyroxenes and their relation to major
 1093 element systematics. **A.** [La/Sm]_n vs. Na in clinopyroxenes from our scoria samples and wehrlite and
 1094 dunite xenoliths ([La/Sm]_n is shown as the composition of melt in equilibrium with each
 1095 clinopyroxene). The black line shows a regression through the data ($r^2 = 0.50$) and the red dashed
 1096 lines show the 95% confidence limits on the regression. The correlation indicates that trace element
 1097 enrichment in the Floreana clinopyroxenes is associated with anomalously high Na contents. **B.**
 1098 [La/Sm]_n vs. [Sm/Yb]_n of melts calculated to be in equilibrium with our Floreana clinopyroxenes
 1099 using the model of Wood and Blundy (1997). The black arrow shows the approximate trend of crystal
 1100 compositional evolution hypothesised to occur as a result of clinopyroxene crystallisation during
 1101 reactive porous flow within the cumulate mush (RPF). The grey field shows whole-rock compositions
 1102 from Fernandina (Geist et al., 2006; White et al., 1993). **B.** additionally shows the whole-rock
 1103 compositions of erupted Floreana lavas (Harpp et al., 2014a) and analyses of the gabbroic xenoliths
 1104 from Floreana (this study). Error bars show the fully propagated 2σ precision of our analyses.



1105

1106

1107

1108

1109

1110

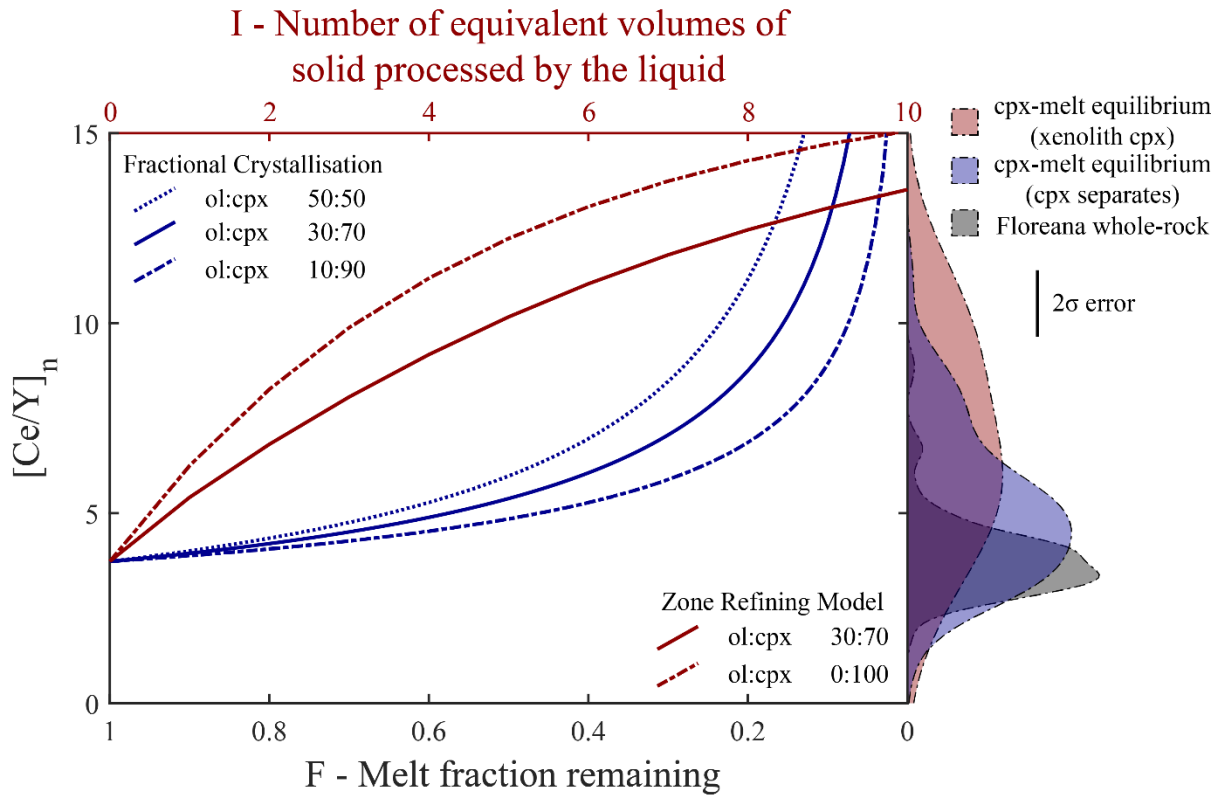
1111

1112

1113

1114

Figure 8 – A. Hierarchical cluster analysis of our clinopyroxene major element analyses. Cluster analysis was performed using Ward’s method, which is built into the scikit-learn package in Python (Pedregosa et al., 2011; Ward, 1963). Height above the x-axis is a measure of the distance of separation of two clusters (i.e., the higher the join the more chemically distinct two clusters are). Colours show the high-level division of crystal compositions into three clusters: Cluster 1 is predominantly comprised of crystals from wehrlite and dunite xenoliths (red), Cluster 2 is composed of crystals from gabbroic xenoliths (yellow) and Cluster 3 (blue) is dominated by crystals separated from scoria samples. **B.** Na vs Mg and **C.** Cr vs Mg in our clinopyroxene analyses from the scoria and xenoliths, coloured by their cluster.



1115

1116

Figure 9 – Models showing the evolution of melt $[Ce/Y]_n$ ratios as a function of the melt fraction

1117

remaining (F) during fractional crystallisation and as a function of the number of equivalent volumes

1118

of solid processed by the liquid (I) during reactive porous flow (red; using the zone-refining model of

1119

Harris, 1957). Line types show how models vary with different ratios of crystallising olivine (ol) and

1120

clinopyroxene (cpx). The kernel density plots show the $[Ce/Y]_n$ density distributions of liquids

1121

calculated to be in equilibrium with clinopyroxene crystals in our wehrlite and dunite xenoliths (red),

1122

scoria samples (blue; 2σ error for the clinopyroxene analyses is shown by the black bar), and whole-

1123

rock analyses of erupted Floreana basalts (grey; Harpp et al., 2014a). Clinopyroxene partition

1124

coefficients were calculated using the method of Wood and Blundy (1997), the mean major element

1125

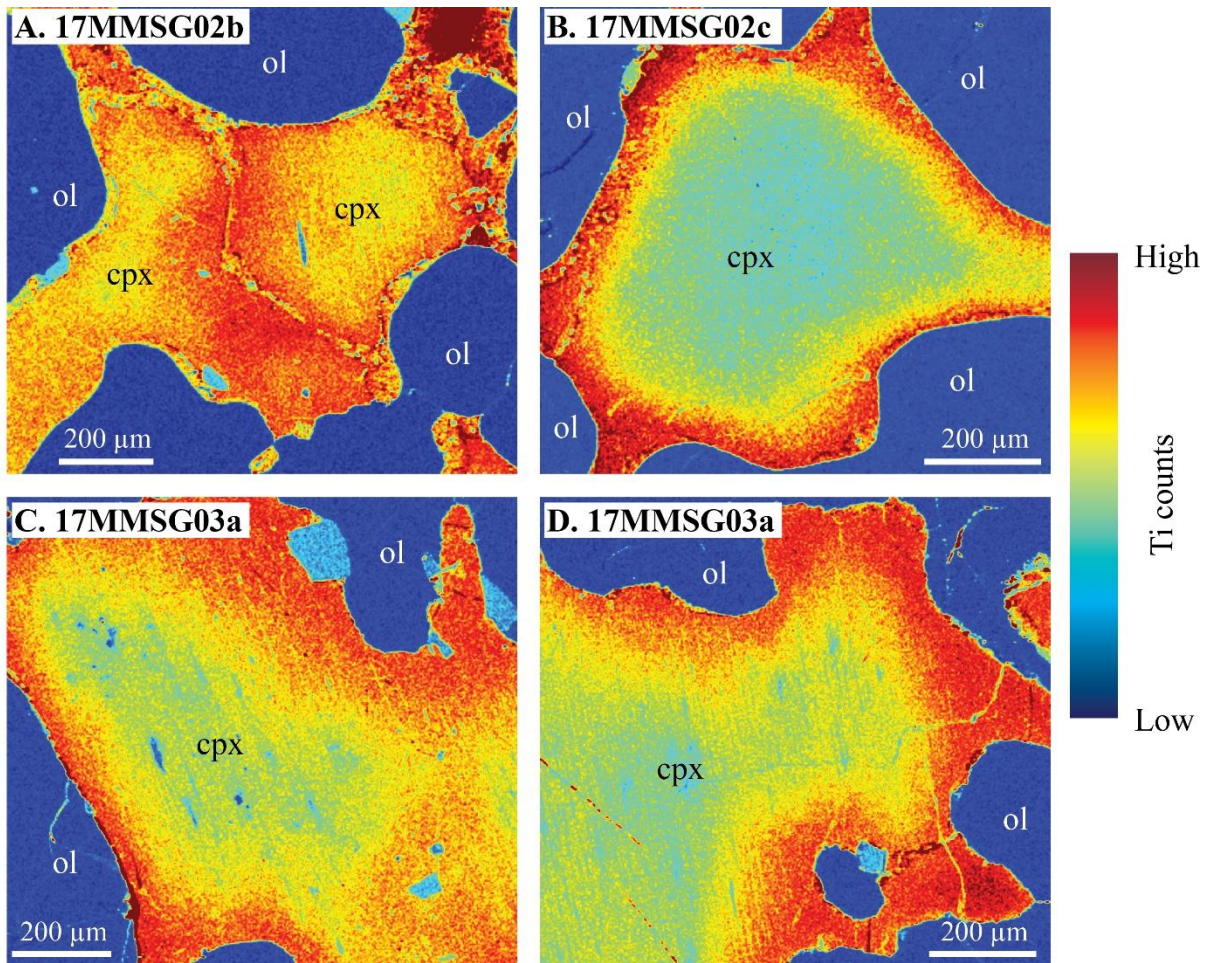
composition of the Cluster 3 clinopyroxenes from this study, a temperature of 1225°C, and a pressure

1126

of 700 MPa. Initial Ce and Y concentrations for both models were taken as the mean values from the

1127

whole-rock dataset of Harpp et al. (2014a). Calculation increments are 0.01 in F and 0.1 in I.



1128

1129

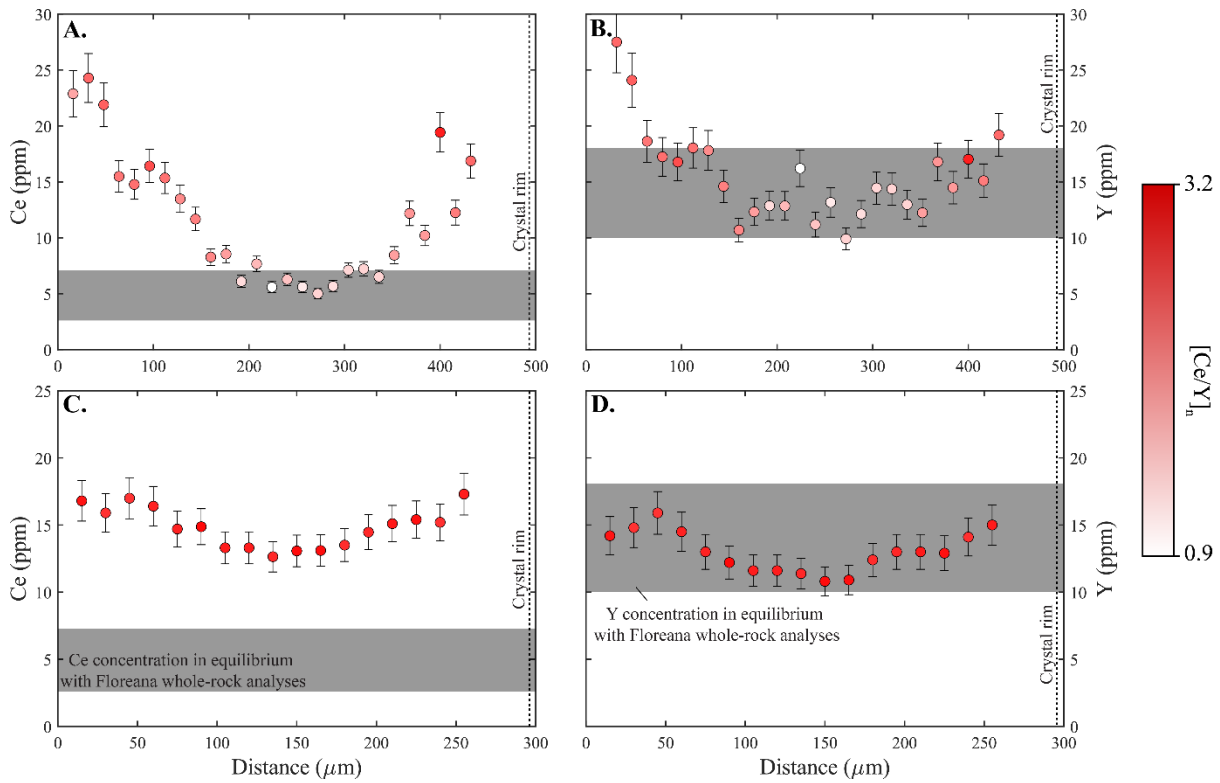
1130

1131

1132

1133

Figure 10 – WDS maps of Ti counts in key clinopyroxene crystals from the Floreana wehrlite xenoliths. These maps display clear zoning in the xenolithic clinopyroxenes with Ti-poor cores and Ti-rich rims. EPMA transects across some of the wehrlitic clinopyroxenes indicates that the Ti concentrations in these crystals may vary from ~0.6 wt% to ~1.3 wt% TiO₂ (see Supplementary Information). The dark blue regions surrounding clinopyroxene grains are olivine crystals.



1134

1135

1136

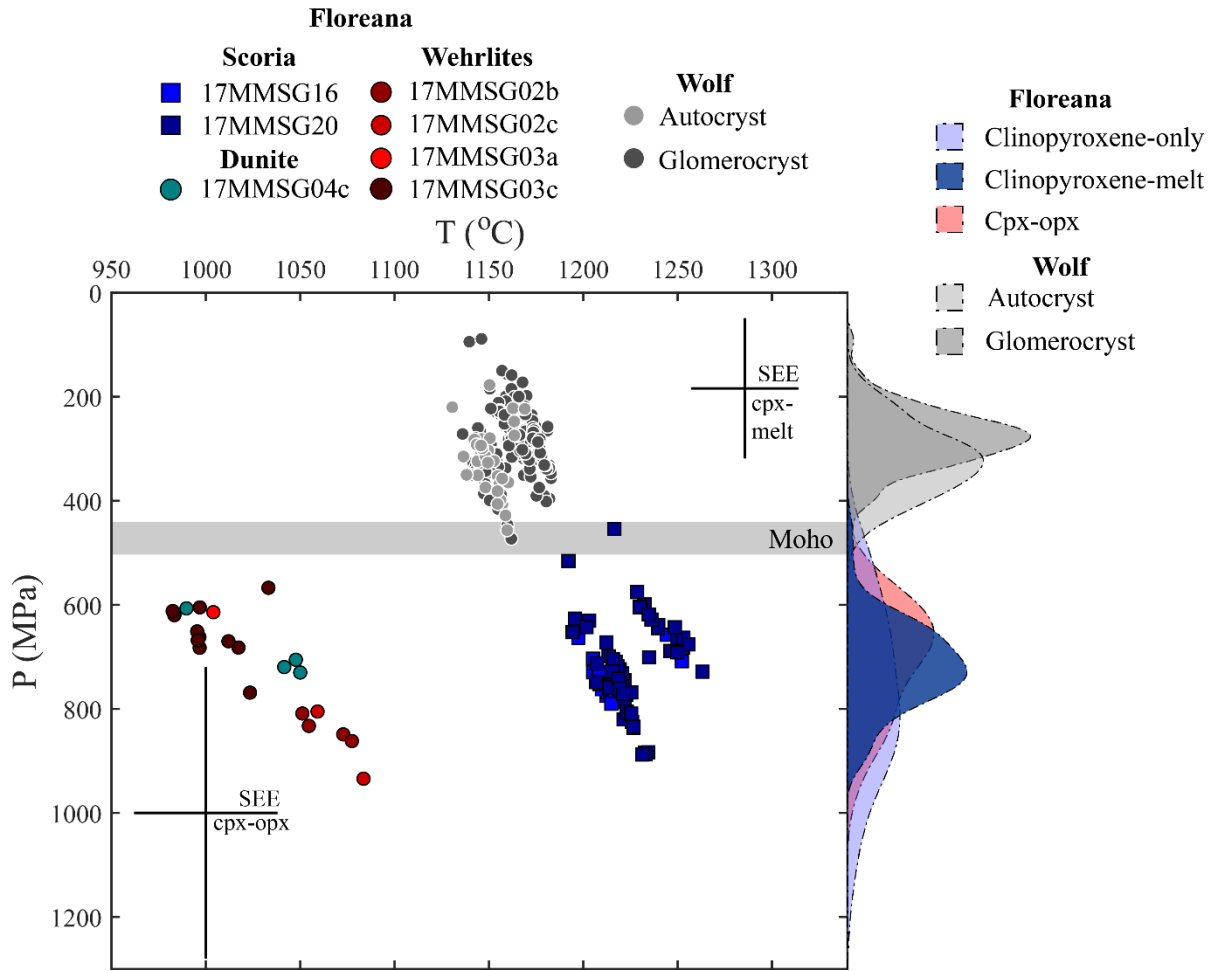
1137

1138

1139

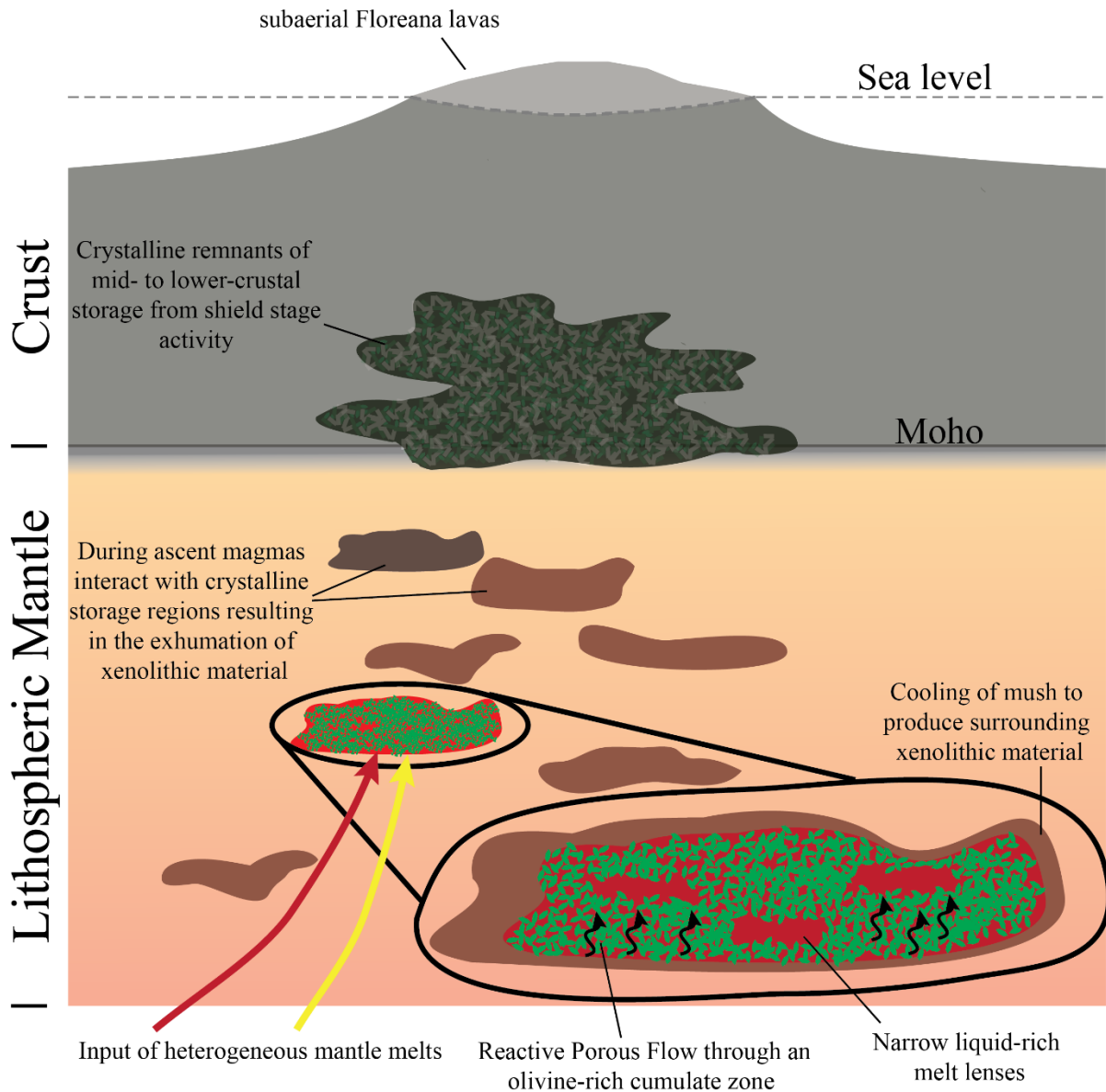
1140

Figure 11 – LA-ICP-MS transects showing Ce (**A, C**) and Y (**B, D**) zoning across two clinopyroxene grains in a wehrlitic xenolith (17MMSG02c). **A.** and **B.** show a transect across the core of a large clinopyroxene oikocryst. **C.** and **D.** show a transect across the apparent core of a smaller clinopyroxene oikocryst. Points are coloured according to their $[Ce/Y]_n$ ratio (see colour scale). The grey bars show the crystal compositions calculated to be in equilibrium with whole-rock analyses of erupted Floreana basalts (Harpp et al., 2014a).



1141

1142 **Figure 12** – Petrological thermobarometry results. The kernel density plots to the right show the
 1143 density distributions of barometric results from different models (light blue – clinopyroxene-only,
 1144 Putirka (2008); dark blue – clinopyroxene-melt, Neave and Putirka (2017); red – clinopyroxene-
 1145 orthopyroxene Putirka (2008)). The grey bar shows the Moho depth beneath Fernandina (from
 1146 Feighner and Richards, 1994) and the grey points and kernel density estimates show clinopyroxene-
 1147 melt thermobarometric results for autocrysts and glomerocrysts from Wolf volcano (from Stock et al.,
 1148 2018). The Standard Estimated Error (SEE) of the clinopyroxene-melt and orthopyroxene-
 1149 clinopyroxene thermobarometers are given.



1150

1151

1152

1153

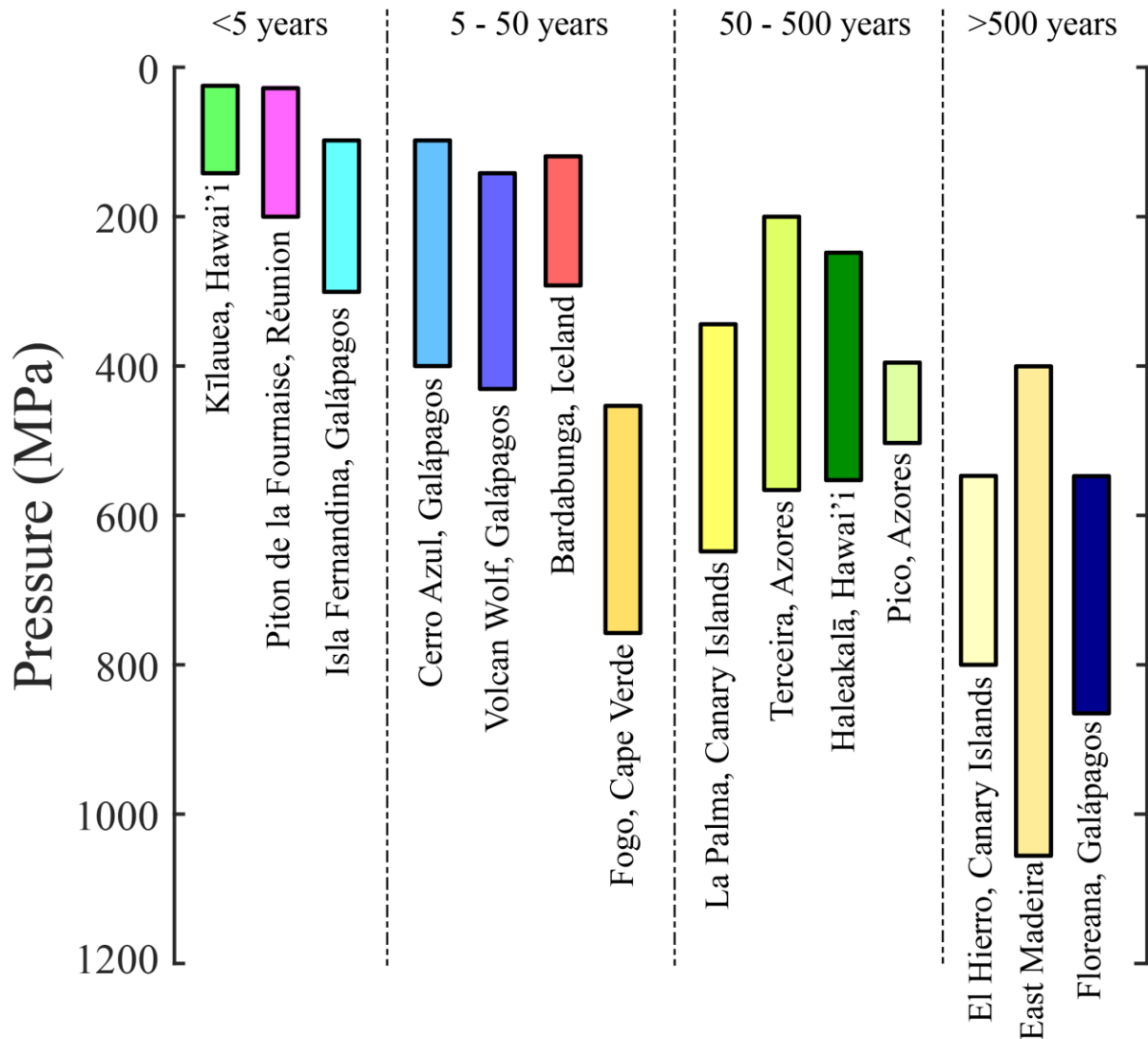
1154

1155

1156

1157

Figure 13 – Schematic illustration of the magma plumbing system beneath Floreana. No magma storage is identified within the crust. Instead, our barometric results indicate that Floreana magmas ascend directly from the upper mantle, where they are stored at a depth of $\sim 23.7 \pm 5.1$ km. Floreana magma storage regions are dominated by crystal-rich domains (i.e. mush). Reactive porous flow is identified as an important mechanism of melt migration and magma differentiation in the crystal-rich storage regions, although our results shows that some crystallisation occurs within liquid-rich domains.



1158

1159 **Figure 14** - Compilation of barometric estimates for the primary magma storage region beneath
1160 various ocean island volcanoes worldwide. Data is divided according to the approximate repose
1161 period between eruptions at each volcano (estimated using data from Global Volcanism Program,
1162 2013), which is used as a proxy for the flux of magma entering the lithosphere. A general trend to
1163 greater magma storage pressures is observed with increasing repose period, indicating that the flux of
1164 magma from the mantle has a first order control on the depth of magma storage. Data from (Famin et
1165 al., 2009; Geist et al., 1998; Hammer et al., 2016; Hartley et al., 2018; Klügel et al., 2015; Poland et
1166 al., 2015; Stock et al., 2018; Zanon et al., 2020; Zanon and Pimentel, 2015).